



Originally published as:

Rybacki, E., Herrmann, J., Wirth, R., Dresen, G. (2017): Creep of Posidonia Shale at Elevated Pressure and Temperature. - *Rock Mechanics and Rock Engineering*, 50, 12, pp. 3121—3140.

DOI: <http://doi.org/10.1007/s00603-017-1295-y>

Creep of Posidonia shale at elevated pressure and temperature

E. Rybacki, J. Herrmann, R. Wirth, G. Dresen

uddi@gfz-potsdam.de

Abstract

The economic production of gas and oil from shales requires repeated hydraulic fracturing operations to stimulate these tight reservoir rocks. Besides simple depletion, the often observed decay of production rate with time may arise from creep-induced fracture closure. We examined experimentally the creep behavior of an immature carbonate-rich Posidonia shale, subjected to constant stress conditions at temperatures between 50° and 200°C and confining pressures of 50 to 200 MPa, simulating elevated in-situ depth conditions. Samples showed transient creep in the semibrittle regime with high deformation rates at high differential stress, high temperature, and low confinement. Strain was mainly accommodated by deformation of the weak organic matter and phyllosilicates and by pore space reduction. The primary decelerating creep phase observed at relatively low stress can be described by an empirical power law relation between strain and time, where the fitted parameters vary with temperature, pressure and stress. Our results suggest that healing of hydraulic fractures at low stresses by creep-induced proppant embedment is unlikely within a creep period of several years. At higher differential stress, as may be expected in situ at contact areas due to stress concentrations, the shale showed secondary creep, followed by tertiary creep until failure. In this regime, microcrack propagation and coalescence may be assisted by stress corrosion. Secondary creep rates were also described by a power law, predicting faster fracture closure rates than for primary creep, likely contributing to production rate decline. Comparison of our data with published primary creep data on other shales suggest that the long-term creep

p [1]

behavior of shales can be correlated to their brittleness estimated from composition. Low creep strain is supported by a high fraction of strong minerals that can build up a load-bearing framework.

Keywords

shale, creep, fracture closure, hydraulic fracturing stimulation, brittleness

List of symbols

$A, B, c_{1,2}, m, t_0, s, k$	Creep constants
B_r	Brittleness
d	Indenter diameter
F	Volume fraction
h, \dot{h}	Indentation depth, rate
n	Stress exponent
P	Confining pressure
Q	Activation energy
T	Temperature
t	Time
V	Activation volume
$\varepsilon, \dot{\varepsilon}$	Axial strain, strain rate
ϕ	Porosity
σ	Differential stress
σ_{net}	Indenter stress

1. Introduction

Over the past 20 years, exploitation of (unconventional) gas from tight shale reservoirs increased strongly and is expected to contribute considerably to future energy supply in the next decades, although estimates of the recoverable amounts of gas are quite variable (Howarth et al., 2011; McGlade et al., 2013). The uncertainty of future production assessment is linked to the difference between the estimated amount of gas in place and the fraction of technically recoverable shale gas resources. Beside socio-environmental issues, fast production decline rates of unconventional gas reservoirs render reliable forecasting very difficult (Hughes, 2013; Wang, 2016). Empirically fitted production curves show a hyperbolic or exponential decline in the first few (four to five) years after stimulation by hydraulic fracturing (Baihy et al., 2010; Wang, 2016). The causes of such a fast decline are a matter of debate and may be related to transient flow of free and adsorbed gas to natural and artificially-induced fractures until (pressure dependent) depletion in conjunction with time-dependent fracture closure (Patzek et al., 2014; Wang, 2016).

A reduction of fracture conductivity with time depends on several factors, including the in-situ closure stress (normally in the range of several tens of MPa acting perpendicular to the fracture surface), fluid chemistry (e.g., brine concentration), fines migration and proppant properties (type, diagenesis, crushing, size and distribution). Experimental and modelling results usually show enhanced fracture closure rates at high closure stress and temperature, low Young's modulus and high amount of soft minerals, low fraction of proppants with small size, low fracture roughness and minor shear displacement (minor self-propping). The presence of water also accelerates the rate of fracture permeability reduction, in particular for clay-rich shales (Akrad et al., 2011; Alramahi and Sundberg, 2012; Guo and Liu, 2012; Kassis and Sondergeld, 2010; LaFollette and Carman, 2010; Liu and Sharma, 2005; Morales p [3]

et al., 2011; Pedlow and Sharma, 2014; Reinicke et al., 2010; Stegent et al., 2010; Volk et al., 1981; Zhang et al., 2013; Zhang et al., 2015; Zhang et al., 2016b). The brittleness of shales, which correlates to some extent with their composition and elastic properties (Rybacki et al., 2016; Zhang et al., 2016a), may be also relevant for the long-term fracture healing rate. Fast healing is expected for more ductile shales by rapid proppant embedment or enhanced creep of contact areas in unproped fractures. In addition, brittleness may control the amount of natural open or sealed fractures, which are generated mainly during subsidence by the pressure increase due to creation of gas or oil from kerogen (Norris et al., 2016).

Quantitative estimates of fracture healing rates require knowledge of the geomechanical behavior of shales. Under reservoir conditions ($P < 100$ MPa, $T < 200^{\circ}\text{C}$), shales often show brittle to semibrittle deformation, where the combination of mechanisms (brittle microfracturing, pore collapse, granular flow and crystal-plastic defect activity) yields a mechanical behavior and strength depending on rock composition and in-situ effective pressure, temperature and strain-rate conditions (Ibanez and Kronenberg, 1993; Rybacki et al., 2015). However, only a few studies of the long-term creep deformation of shales exist so far. Few data exist dealing with the creep behavior of Opalinus clay (Naumann et al., 2007), Boom clay (Yu et al., 2015), Callovian-Oxfordian Bure Clay (Gasc-Barbier et al., 2004), and other argillaceous rocks (Zhang and Rothfuchs, 2004; Fabre and Pellet, 2006). Creep experiments on shales focus on compaction and consolidation (Cogan, 1976; de Waal and Smits, 1988; Dudley et al., 1998), the effect of adsorption and swelling on creep (Heller and Zoback, 2011; Hol and Zoback, 2013) and on viscoelastic or viscoplastic creep of shales in response to nanoindentation (Mighani et al., 2015) and applied differential stresses at elevated confining pressures (Almasoodi et al., 2014; Chang and Zoback, 2009, 2010; Chong et al., 1978; Li and Ghassemi, 2012; Rassouli and Zoback, 2015; Sone and Zoback, 2010, 2011; Sone and Zoback, 2013, 2014; Yang and Zoback, 2016). The latter experiments indicate that

creep is enhanced at high differential stress, high clay content, in the presence of water and if loaded normal to bedding orientation. For the examined North American shales the influence of confining pressure appears to be either absent or reducing creep rates only slightly up to a few tens MPa confinement.

Here, we report on deformation experiments on immature Posidonia (oil) shale at high confining pressures (P) and temperatures (T) in order to evaluate the creep properties of this relatively weak shale as a function of stress and applied P - T conditions. The results are used to estimate the proppant embedment potential and fracture closure from measured long-term creep behavior.

2. Sample Material and Experimental Methods

Cylindrical samples of 20 mm length x 10 mm diameter were prepared from black shale blocks collected in a quarry with active mining near the village Dotternhausen (Southern Germany). This immature Posidonia shale (vitrinite reflectance $\approx 0.6\%$) of Mesozoic (lower Jurassic) age is very fine-grained ($< 10\ \mu\text{m}$) with a porosity of about 11%, measured by mercury injection porosimetry (Fig. 5 a). The pore throat diameter distribution shows a maximum between 20 and 40 nm. The laminated matrix of this carbonate mudstone consists of $\approx 42\ \text{vol}\%$ carbonates, 18 vol% clays (illite, illite-smectite mixed layers and minor kaolinite and chlorite), 14 vol% quartz, feldspar and pyrite and 15 vol% organic matter with high bitumen content (Rybacki et al., 2015). All samples were drilled perpendicular to bedding, defined by enrichment in organic matter with subparallel oriented pyrite flakes and calcareous bands. The as-is water content of samples is 1-2 wt%. They were stored in an oven at 50°C until testing.

Triaxial creep experiments were performed in a Paterson-type deformation apparatus (Paterson, 1970) at constant load, using argon gas as confining pressure medium. Samples were jacketed by 0.5 mm thin copper sleeves to prevent intrusion of the gas, pressurized and heated to the desired level, and deformed in a single run to maximum axial strains between 3% and 26%, depending on applied P - T conditions (Tab. 1). Recorded axial displacements were corrected for the system compliance, resulting in calculated axial strains with an uncertainty $< 4\%$. Measured axial forces were corrected for the strength of copper sleeves, previously determined in calibration runs on copper samples at similar conditions, and converted to axial stress assuming constant volume deformation. Because of the low stiffness of the Paterson apparatus the initial elastic stress is less accurate with an estimated error $< 20\%$. The reported error of post yield stress is typically $< 6\%$ at $T < 200^\circ\text{C}$ and $< 10\%$ at $T = 200^\circ\text{C}$, resulting from uncertainty of the copper strength, which depends on P - T conditions and strain rate, and slightly decreasing sample stress with increasing strain at fixed applied load. The copper strength was in the range of 204 to 380 MPa, accounting for $21 \pm 4\%$ of the measured total force.

For examination of microstructures we used a scanning electron microscope (SEM, Zeiss Ultra 55 Plus) on broad ion beam (BIB, Jeol IB-19520CCP) polished sections. High resolution analysis was done using a transmission electron microscope (TEM, Fei Tecnai G2 F20 x-Twin) on focused ion beam (FIB, Fei FIB200TEM) prepared foils.

3. Results

In total, we performed 20 creep tests on samples at confining pressures of 50-200 MPa and temperatures between 50 and 200°C . The applied differential stresses (corrected for jacket strength) were between ≈ 60 and 205 MPa, resulting in transient creep curves. Tests were

either manually stopped after some time or beyond sample failure after passing a secondary and finally accelerating creep phase, depending on conditions. The corresponding total creep time varied between 1 minute and 165 hours (≈ 1 week) and the associated axial strain between ≈ 3 and 26% (Tab. 1). In most tests the conditions were chosen such that 2 of the 3 parameters (confinement, temperature, differential stress) were fixed and the third parameter was changed in order to constrain the influence of the varying parameter on the resulting creep rate.

3.1 Creep Behavior

Some typical creep curves of deformed Dotternhausen shales are shown in Fig. 1. At constant pressure and temperature, creep rates increased with increasing differential stress, independent of the specific P - T conditions (Fig. 1 a-d). Samples subjected to low differential stress showed primary creep behavior, where the strain increment per unit time step continuously decreases with increasing time (primary or decelerating creep phase). In contrast, samples loaded at high differential stress showed subsequently secondary creep with a linear increase in strain with increasing time (i.e. constant creep rate) and finally tertiary (accelerating) creep until failure. The transition from primary to secondary creep occurred in a narrow stress range, corresponding to about 84-90% of the compressive strength obtained in constant strain rate tests of $5 \times 10^{-4} \text{ s}^{-1}$ under similar P - T conditions (Rybacki et al., 2015). Reproducibility was high at low stress, but decreased at high stress deformation (Fig. 1a). An increase of confining pressure at constant temperature and stress yielded a decrease of creep rate, i.e., strengthening (Fig. 1e). In contrast, increasing temperature at constant confinement and stress resulted in weakening, i.e., increasing creep rate (Fig. 1f). We conclude that the creep behavior of Posidonia shale at elevated P - T conditions is sensitive to stress, pressure and temperature, as expected for semibrittle deformation.

An example of calculated strain (creep) rates of samples deformed at 50 MPa confinement and 100°C temperature (DOT01-DOT04, Tab. 1), are shown in Fig. 2. Here, we show smoothed curves since the numerical derivation of strain rate from strain-time curves yielded noisy results. For comparison, two exemplary unsmoothed curves are shown in light gray in Fig. 2a. The two low stress samples deformed in the primary creep regime at 148-150 MPa stress show continuously decreasing strain rates down to about 10^{-8} s^{-1} until test termination, even after about 1 week deformation (sample DOT 04, deformed at $\sigma = 148 \text{ MPa}$). The other two samples deformed at higher stress experienced minimum creep rates of about 10^{-5} s^{-1} before failure (Fig. 2a, Tab. 1).

We fitted several suggested creep laws to our laboratory-derived creep curves (duration < 1 week). Some commonly used empirical laws describing time-dependent strain from primary creep are:

$$\text{parabolic: } \varepsilon = At^m \quad (1)$$

$$\text{logarithmic: } \varepsilon = A + B \log(t) \quad (2)$$

$$\text{exponential: } \varepsilon = A(1 - Be^{-t/t_0}) \quad (3)$$

$$\text{hyperbolic: } \varepsilon = A \sinh \left[(Bt)^s \right] \quad (4)$$

$$\text{crack-damage: } \varepsilon = Ae^{-B/\ln(kt)} \quad (5)$$

with ε = strain, t = time, and A, B, m, t_0, s, k = constants. Equations (1) - (4) have frequently been used to describe the decelerating transient behavior of rocks, soils and metals (Findley et al., 1976; Gupta, 1975; Karato, 2008; Paterson, 2013; Stouffer and Dame, 1996). Recently, Brantut et al., 2013 suggested eqn. (5) to express crack-damage related brittle creep of rocks. In terms of strain rate - time relation, the power-law creep equation (1) predicts a slope of $m-1$

in a double-logarithmic plot. For logarithmic creep (eqn 2) the slope of strain rate versus time should be -1, which does not agree with our measurements (Fig. 2a). For the exponential creep law (eqn 3), the logarithmic strain rate should decrease linearly in time. However, a constant slope of $-\log(e)/t_0$ does not match our results that rather suggest a non-linear relationship (Fig. 2b). The exponential creep equation 3 is based on the Zener rheological model. This phenomenological model is composed of a combination of linear elastic springs and a linear viscous dash-pot (i.e., the standard linear solid). If the mechanical behavior does not depend on deformation history, a mechanical equation of state may exist and the relation between strain and strain rate can be described in the form $\varepsilon = A\dot{\varepsilon}^r$, where $\dot{\varepsilon}$ is strain rate and A and r are constants (Hart, 1970; Karato, 2008). In double-logarithmic space this would result in a linear relation with slope r , in contrast to what is suggested by our measurements (Fig. 2c). This implies that the creep behavior of shales does indeed depend on deformation history and stress path, as expected for porous rocks.

Using a non-linear fitting procedure, we fitted eqns. (1) – (5) to the creep curve of sample (DOT04). The test performed on this sample had the longest duration of about 1 week (Fig. 2d). The corresponding fit-parameters A , B , m , t_0 , s , k and the fitting determination coefficients (r_{fit}^2) for the whole (inelastic) test duration of ≈ 1 week are given in Tab. 2. The best fit with highest r_{fit}^2 is obtained by the hyperbolic creep law, in descending order followed by the parabolic, crack-damage, logarithmic and finally exponential relationship (Tab. 2). Except for the Zener model, all others show a relatively good match with the data at test durations ≥ 5 hours, whereas for shorter duration the misfit increases (Fig. 2d). To compare results from all low stress experiments performed at different boundary conditions and terminated after different times, we refitted sample DOT04 in the time interval 50-5000 s. This interval of ≈ 1.4 h covers the duration of all low stress experiments except one (Tab. 1). It corresponds roughly to a strain difference of 1% for all low stress tests. The determined fit

parameters are listed in Tab. 2, revealing slightly different values than those obtained after 1 week duration.

Extrapolation of the experimental data using the fit parameters to estimate the strain accumulated after 3 years creep duration yields extrapolated strains between 0.112 and 0.069 (Tab. 2). A time period of 3 years is the typical time interval between refrack operations in unconventional reservoirs. Likely, the hyperbolic fit for 1 week test duration best represents the creep behavior with a resulting creep strain of 0.112 (here set to 100%). Extrapolation from this fit is taken as the reference strain accumulated after 3 years. Extrapolating strain using a hyperbolic fit to a 1.4 h test interval yields a strain of 0.091, i.e., 11.6% less than the reference strain. In the following, for simplicity we use the power law fit (eqn. 1) to data from all tests. Compared to the hyperbolic fit the strain extrapolated to a creep period of 3 years using the power law is 7.1% (1 week fit) and 19.6% (1.4 h fit) less than the reference strain.

The power law fit parameters A and m for all tests showing mainly primary creep are given in Tab. 1. They vary for A between 0.015 - 0.062 s^{-m} and for m between 0.046 - 0.107, depending on deformation conditions. For samples that showed also secondary and tertiary creep until failure, power law parameters for primary creep for the same time interval of 50-5000s could not be estimated because most samples failed earlier (Tab. 1).

To our knowledge no microphysical models for semibrittle creep of multiphase materials exist, which allow predicting stress, temperature and pressure dependence of A and m . Inspection of the experimental data (Fig. 1, Tab. 1) suggests that parameters A and m in equation 1 increase with increasing stress and temperature and with decreasing confining pressure. To fit the data we use a modified constitutive power law commonly used to describe the steady state creep rate (cf., eqn. 9) in the high temperature (ductile) regime. Here we account for the

observed dependence of parameters A and m on stress, temperature and pressure using the

relations $A = A_0 \sigma^{n_1} e^{-\frac{Q_1 + P \cdot V_1}{R \cdot T}}$ and $m = m_0 \sigma^{n_2} e^{-\frac{Q_2 + P \cdot V_2}{R \cdot T}}$ which yields:

$$\varepsilon = A t^m = A_0 \sigma^{n_1} e^{-\frac{Q_1 + P \cdot V_1}{R \cdot T}} t^{m_0 \sigma^{n_2} \exp\left(-\frac{Q_2 + P \cdot V_2}{R \cdot T}\right)} \quad (6)$$

where n is stress exponent, Q is activation energy (in kJ/mol), V is activation volume (in cm³/mol), σ is stress (in MPa), T is (absolute) temperature (in K), P is pressure (in GPa) R is the (molar) gas constant and A_0 , m_0 are rock-specific constants. In this approach, we assume that the combined operation of microphysical processes accommodating semibrittle flow of shales like dislocation slip, microcracking, granular flow, bending of sheet silicates and compaction are captured phenomenologically. The stress, temperature and pressure dependence of A and m may be also described by other relationships, but eqn (6) allows comparing the derived parameter-sensitivities to the results of high temperature creep of rocks. Taking the logarithm of eqn (6) yields the following relations between A and m and σ , T and P :

$$\log(A) = \log(A_0) + n_1 \cdot \log(\sigma) - \frac{Q_1 \cdot \log(e)}{R \cdot T} - \frac{P \cdot V_1 \cdot \log(e)}{R \cdot T} \quad (7)$$

$$\log(m) = \log(m_0) + n_2 \cdot \log(\sigma) - \frac{Q_2 \cdot \log(e)}{R \cdot T} - \frac{P \cdot V_2 \cdot \log(e)}{R \cdot T} \quad (8)$$

where the subscripts 1 and 2 are used for the stress, temperature and pressure sensitivity of A and m , respectively. Figure 3 shows the corresponding plots of 10 measurements, for which at least two of the three parameters T , P and σ were fixed in the experiments (linked by dotted lines). The 11th measurement on sample DOT12 was neglected in the analysis, because it was performed at relatively high stress yielding an exceptionally high A value (Tab. 1). Data sets for $\log(A)$ and $\log(m)$ were fitted by multiple linear regression (broken lines in Fig. 3). Since m appears to be insensitive to stress (Fig. 3 b), we fixed $n_2 \equiv 0$ (best fit estimate is $n_2 = -0.03$ p [11])

± 0.03). In addition, the pressure-sensitivity of was fixed to $V_I = 0.92 \text{ cm}^3/\text{mol}$ based on the almost linear slope shown in Fig. 3e (the best fit for all data would slightly increase this value to $3.01 \text{ cm}^3/\text{mol}$). The remaining fit parameters n_I , Q_I , A_0 and Q_2 , V_2 , m_0 are given in Fig. 3 and Tab. 3. In general, the calculated regression lines show a good fit to the data, particularly for A and somewhat less for m .

Comparing strains extrapolated to 3 years creep period yields similar estimates (deviation $< 0.1\%$) for multilinear fit and for values determined directly from A and m parameters given in Tab. 1. The standard deviation is 37%. This is comparable to the uncertainty related to the choice of constitutive equation (eqns. 1-5) which is also possibly affected by sample to sample variations. Since sample diameter increases with increasing strain at fixed load the applied stress decreased by 2-5 MPa between yield point and test termination. Accounting for this effect on extrapolation reduces 3 year strain estimates by about 3-7%.

For extrapolation of strains from samples tested at high stresses, we calculated the minimum creep rates $\dot{\epsilon}_{\min}$ (Fig. 2a and Fig. 1a-c). The resulting set of strain rates are given in Tab. 1. The σ , T and P - dependence of $\dot{\epsilon}_{\min}$ was fitted to a power law creep equation used for dislocation creep in rocks and metals (Karato, 2008; Paterson and Wong, 2005):

$$\dot{\epsilon}_{\min} = B_0 \sigma^{n_3} e^{-\left(\frac{Q_3 + P V_3}{R T}\right)} \quad (9)$$

where B_0 is a material constant and the subscript 3 denotes the stress, temperature and pressure sensitivity for steady state creep. As for the primary creep regime, application of eqn (9) to the semibrittle deformation regime is empirical and this relationship does theoretically not capture deformation processes other than dislocation creep. Taking as before the logarithm of eqn (9) yields:

$$\log(\dot{\epsilon}_{\min}) = \log(B_0) + n_3 \cdot \log(\sigma) - \frac{Q_3 \cdot \log(e)}{R \cdot T} - \frac{P \cdot V_3 \cdot \log(e)}{R \cdot T} \quad (10)$$

Using eqn (10) we fitted the measured minimum strain rates by multilinear regression yielding the parameters given in Tab. 3. It should be noted that uncertainties for the fitted parameters are high, presumably because the data obtained at 50 MPa pressure and 100°C temperature (samples DOT 01, 03) appear to be very strong compared to the others. Accordingly, the error between measured and fitted strain rate is large (more than one order of magnitude) for some samples (Fig. 4).

3.2 Microstructures

Microstructures of starting material and deformed samples were investigated using scanning electron microscope (SEM) and transmission electron microscope (TEM) observations. In general, the microstructures as observed in SEM show only few changes compared to the starting material. For samples deformed in the primary creep regime, some samples show indentation of strong minerals into weaker phases (e.g., quartz into apatite, Fig. 5 b), and bending of clays and mica (Fig. 5c). Samples that were deformed at higher stress until failure show formation of inter- and intracrystalline microcracks (Figs. 5 d and e, respectively). Note stretching of pyrite framboids by deformation-induced sliding of microcrystallites (Fig. 5 d). Pore collapse is also observed, in particular close to the macrofracture formed during sample failure (Fig. 5 f), which is usually inclined by $35 \pm 2^\circ$ with respect to the sample axis. This friction angle corresponds to a friction coefficient μ of 0.70 ± 0.05 and is considerable higher than observed in constant strain rate tests on similar shale ($\mu \approx 0.2$, (Rybacki et al., 2015)).

TEM microscopy also reveals pore collapse in between calcite flakes under stress (Fig. 6 c, f). The latter are partially crushed into small fragments (Fig. 6 g). Larger calcite grains are

enriched in Sr (Fig. 6 a, c). In highly strained regions, framboidal pyrite initially containing pores and S-enriched organic matter is fragmented and sheared (Fig. 6 e). Clay minerals (mainly illite and kaolinite) are bent and wrapped around stronger quartz and calcite grains (Fig. 6 b, h). In cases voids exist between clay flakes in face-to-face contact (Fig. 6 f, top). Larger quartz aggregates are composed of fine grains with inclusions decorating grain boundaries (Fig. 6 g). Few stretched Fluor-apatite grains consist of very small (≈ 50 nm long) grains (Fig. 6 d) that are occasionally embedded by calcite grains (Fig. 6 b). High resolution TEM (not shown here) demonstrates that apatite is partially amorphous. Interestingly, all inspected grains are nearly free of dislocations (Fig. 6 h) and just some larger calcite grains show few twins and low angle grain boundaries (not shown here).

4. Discussion

The time-dependent (inelastic) creep strain response to an applied constant load is subdivided into primary, secondary and tertiary creep. Here, we discuss observations from shale samples deforming in primary and secondary creep regime, as indicated by mechanical data and microstructure observation.

4.1 Deformation Mechanisms and Constitutive Equations

The laboratory deformation experiments on Posidonia shale at elevated pressure and temperature reveal different creep behavior and deformation mechanisms, depending on applied stress and P - T conditions. For axial stresses less than 84-90% of the short term compressive strength, samples deformed by primary creep with continuous hardening leading to a progressive strain rate reduction with increasing time and strain. The microstructural observations suggest that creep strain is primarily accommodated by deformation of the weak p [14]

mineral and organic constituents (clays, organic matter), and pore space reduction. This may have involved frictional sliding of very fine mineral grains. Where present, organic material likely acts as a lubricant between grains and clays are expected to allow easy glide along aligned platy aggregates.

At higher stress, samples show apparent steady state and finally accelerating deformation, leading to shear failure. Deformation is locally accommodated by pronounced pore collapse and formation of inter- and intracrystalline microcracks. Progressive crack coalescence likely leads to macroscopic failure of samples. The Posidonia shale tested in this study contains a cumulative fraction of organic matter, clays and pores of about 44 vol% accommodating most of the strain. Crystal plastic deformation is limited to bending and intracrystalline gliding of clay layers and twinning in calcite grains.

Since the samples were not dried, chemical reactions may also lead to subcritical crack growth by stress corrosion. Time dependent creep strain and static fatigue of brittle rocks were explained by this thermally activated mechanism, where the crack velocity depends on humidity, stress intensity factor at the crack tip and temperature (e.g., Atkinson and Meredith, 1987; Ciccotti, 2009; Kranz, 1980; Kranz et al., 1982; Heap et al., 2009a, 2009b). We expect that stress corrosion at least partially contributed to creep of our samples, although this cannot be verified by microstructural observations. High stress samples were deformed at about 84-90% of the short-term compressive strength indicating that dilatant behavior may have been initiated if compared to brittle creep of porous sandstone at room temperature, where the onset of dilatancy requires stresses less than 80-90% of the compressive strength (Heap et al., 2009a). Unfortunately, we were not able to measure volumetric strain during the experiments allowing to record a potential onset of dilatant behavior of samples deformed under high stress.

Primary creep is usually described by empirical mechanical models that consist of a combination of elastic (spring) and viscous (dashpot) elements for viscoelastic creep (Hagin and Zoback, 2004; Karato, 2008; Masuti et al., 2016; Paterson, 2013), which may be complemented by plastic (sliding friction) bodies, e.g. (Bonini et al., 2007; Jiang et al., 2013). These rheological models are often applied to high-temperature dislocation and diffusion creep of rocks and metals. The models do not account for brittle processes like microcrack formation and propagation, which may lead to cataclastic or granular flow. Mainly for deformation in the brittle field, microcrack damage evolution and stress corrosion was related to transient creep (Bikong et al., 2015; Brantut et al., 2012; Brantut et al., 2014; Brantut et al., 2013; Fjær et al., 2014; Heap et al., 2009a; Li and Shao, 2016). Most of these models suggest a parabolic, logarithmic or exponential constitutive equation for brittle creep (e.g. equation (5) as above).

For steady state creep of rocks and metals, a flow law as in eqn. (9) is commonly applied to describe deformation accommodated dominantly by dislocation activity and diffusion of point defects (Frost and Ashby, 1982; Karato, 2008; Ranalli, 1987). For brittle creep of rocks controlled by stress corrosion, the relation between minimum creep rate in the secondary regime and applied stress can be similarly described in a power law form (Heap et al., 2009; Brantut et al., 2012). However, as observed here, semibrittle deformation of shales involves a complex interplay of several micromechanisms. The respective contributions of each mechanism may change with progressive strain. In particular if crack damage accrues leading to final failure, the time dependence of the secondary (steady state) creep interval may be regarded as a minimum rather than a steady state creep rate that would allow continuous deformation without failure (Brantut et al., 2012; Main, 2000; Wilshire and Burt, 2008).

We are not aware of any constitutive equation that describes primary or secondary creep in the semibrittle field. Due to the complexity of deformation mechanisms acting together during

creep of multiphase shales, their mechanical behavior may be described by empirical laws such as eqns. (6) and (9). This approach is regarded to be acceptable to study fracture healing properties since experimental pressures and temperatures are similar to in-situ values and the dominant micromechanisms accommodating deformation are not expected to change between experimental duration and time intervals of several years relevant in the field. Also, differential stresses applied in experiments are expected to reflect the enhanced stresses induced by proppant embedment or in the load-bearing parts of self-propped fractures.

4.2 Effect of Stress, Pressure and Temperature on Primary Creep

4.2.1 Effect of Stress

For primary creep, we used the power law description of creep strain as a function of time (eqn. (6)). Fitting eqn. 6 to our data from tests performed at different pressures and temperatures indicates that the stress dependence n_2 in the power law (expression for the time exponent m) vanished. The parameter A depends on stress raised to a power of $n_1 \approx 1.4$ (eqn. (6), Tab. 3). This result suggests that creep shows a non-linear dependence on stress, i.e., creep is not Newton-viscous, for which n_1 would be equal 1. In contrast, creep experiments on a number of American shales (Barnett, Haynesville, Marcellus, Eagle Ford, Fort St. John, Bakken, Three Forks, Lodgepole) showed linear-viscous behavior instead (Almasoodi et al., 2014; Li and Ghassemi, 2012; Rassouli and Zoback, 2015; Sone and Zoback, 2013, 2014; Yang and Zoback, 2016). However, in these earlier studies the applied differential stresses ($\sigma < 90$ MPa, mostly < 40 MPa) and the confining pressures ($P < 60$ MPa, mostly 15-40 MPa) were substantially lower compared to our tests performed at pressures $P \geq 50$ MPa and stresses $\sigma \leq 200$ MPa (Tab. 1). Only for Marcellus shale deformed at $P = 19$ MPa viscosity was reported to become nonlinear for $\sigma > 80$ MPa (Li and Ghassemi, 2012). In addition,

maximum strains achieved in these tests were relatively low (usually $< 10^{-4}$) compared to our study with inelastic strains $> 10^{-2}$.

Unfortunately, no deformation mechanisms were reported in the studies cited above. We speculate that pore space compaction and closing of preexisting microcracks may have accommodated much of the measured strain, whereas in our experiments other additional processes (plastic deformation of weak phases, grain boundary sliding and limited microcracking) were active, likely resulting in stress exponent n_I higher than 1. In addition, almost all experiments on North American shales were performed by stepwise increasing the stress, which may have influenced subsequent creep steps at higher loads due to the irreversible modifications of the microstructure in preceding steps at low loads. This approach may have resulted in lower strain rates than would be obtained in single runs at constant stresses as presented here. Accordingly, the expected stress sensitivity n_I in our tests is likely higher than that reported on shales in the literature.

4.2.2 Effect of Pressure

We observed that increasing confining pressure reduced the total strain accumulated per time during primary creep of Posidonia shale (Fig. 1e). This indicates that strength increased with increasing confining pressure as expected for the semibrittle behavior of this shale (Rybacki et al., 2015). The strengthening effect is presumably caused by enhanced compaction of voids and microcracks with increasing pressure. Also, frictional sliding of grains at high P is expected to contribute less to deformation. The effect of pressure on crystal plastic deformation (of the weak phases) is usually small, yielding activation volumes for high temperature steady state creep rate of common silicates in the range of $\approx 10\text{--}40 \text{ cm}^3/\text{mol}$ (Bürgmann and Dresen, 2008). Interestingly, we obtained $V_2 \approx 11 \text{ cm}^3/\text{mol}$ as pressure sensitivity of m in low temperature transient creep of shales, which is of the same order as for high-temperature creep of silicates. In contrast, V_I is close to zero as is the measurement error

p [18]

indicating that the influence of pressure on A is minor or even negligible (Tab. 3). It should be recalled, however, that the tested shales deformed in a semibrittle regime. Therefore, we point out that the exponential pressure dependence of primary creep strain expressed by an activation volume is purely empirical. The estimated pressure dependence may not capture the pressure sensitivity of brittle deformation mechanisms resulting in pore space compaction or dilatant microcracking. Using activation volumes V_1 and V_2 , the pressure-related creep strain after 3 years at a temperature of 75°C and stress of 30 MPa would be reduced by about 11% if pressure increased from 50 to 75 MPa (corresponding to a stress change from 2 to 3 km depth, respectively), which is mainly related to the reduction of m . For comparison, for an increase in differential stress at depth from 30 to 40 MPa, creep strain accumulated after 3 years is about 48% larger. It is interesting to note that low stress - low strain creep tests performed on Barnett, Haynesville, Eagle Ford and Fort St. John seem independent of confining pressure between $P = 10$ and 60 MPa (Sone and Zoback, 2013, 2014). Creep strain even increased with increasing confinement at $P = 0.1 - 19$ MPa for Barnett, Haynesville and Marcellus shale (Li and Ghassemi, 2012). This is in stark contrast to our observations. In those studies tests were performed at lower pressures and stresses compared to the ones presented here. It is conceivable that in those studies shear enhanced compaction significantly increased with increasing confinement (Almasoodi et al., 2014). Instead in our tests performed at relatively higher pressures, samples may have already compacted during the isostatic pressurization stage prior to axial loading.

4.2.3 Effect of Temperature

To our knowledge, the influence of temperature on creep of shales was not investigated so far. Constant strain rate tests on shales at elevated pressure and temperature show that the strength decreases with increasing temperature as expected for deformation that involves plastic processes (Ibanez and Kronenberg, 1993; Rybacki et al., 2015). We also observed increasing

primary creep strain with increasing temperature (Fig. 1f), presumably related to the temperature sensitivity of deformation of weak phases. However, the obtained activation energies of $Q_1 \approx 2.5$ kJ/mol and $Q_2 \approx 4.8$ kJ/mol are very low compared to values for high-temperature plasticity of silicate rocks, which typically amount to hundreds of kJ/mol for dislocation or diffusion creep, depending on composition, water content and dominating deformation mechanism (Bürgmann and Dresen, 2008). For creep of fine grained carbonates Q is about 200 - 300 kJ/mol e.g., (Rybacki et al., 2003), for mica ≈ 50 - 90 kJ/mol (Ibanez and Kronenberg, 1993) and for bitumen ≈ 145 kJ/mol (Mouazen et al., 2011). Stress corrosion, which is also temperature sensitive, yields Q -values between 30 and 50 kJ/mol in the secondary regime (Brantut et al., 2012), which is also higher than Q_1 and Q_2 . The difference to the low Q values obtained in this study may partially arise from the comparison of transient with steady state deformation conditions and from the nature of predominant deformation processes, which in case of shale deformation is a combination of plastic and brittle mechanisms. Semibrittle deformation likely has relatively low temperature sensitivity since the brittle mechanisms involved are much less affected by T than thermally activated plastic deformation (Lockner, 1995). In line with that, we observed only a minor dislocation activity in our samples, indicative of high temperature creep deformation. In addition, partial dehydration of clay minerals may have occurred at high temperature, depending on local pore fluid pressure. If so, it may have contributed to the observed temperature sensitivity of creep curves.

It should be noted that we used total strain for derivation of parameters n , Q and V . Since the total strain includes elastic deformation, these parameters, in particular n , will change if restricted to inelastic strain and may then reflect better microphysical creep processes. Here, we prefer using total strain allowing easy comparison with known literature data and extrapolation to natural conditions.

4.3 Effect of Composition, Orientation and Brittleness on Primary Creep

To estimate the influence of shale composition on primary creep, we used a slightly modified form of the power law creep equation (1):

$$\varepsilon = B\sigma^n t^m \quad (11)$$

where A in eqn. (1) is replaced by $B \cdot \sigma^n$ to be able to compare our data with data available in the literature. For Barnett, Haynesville, Eagle Ford and Marcellus shale we calculated average B and m values from published creep data provided by (Li and Ghassemi, 2012; Rassouli and Zoback, 2015; Sone and Zoback, 2014). Mean values determined for bedding-normal and, if available, bedding-parallel deformation are summarized in Tab. 4, together with the approximate composition. As mentioned above, these authors measured the creep behavior at room temperature at low confining pressure and stress. For comparison to our data we set $P = 20$ MPa in line with the approximate pressure used. Note that these authors did not find any dependence of creep strain on pressure (see above) and that they measured linear-viscous creep with $n = 1$.

The resulting total creep strain after 3 years deformation at an applied stress of 30 MPa is given in Tab. 4 and plotted in Fig. 7 in relation to shale porosity, volumetric fraction of clay plus organic matter (ClyTOC), carbonates (Cb), and fraction of strong minerals (QFP = quartz + feldspar + pyrite). As expected from microstructural observations, the creep strain increases strongly with increasing porosity, although the error due to averaging is relatively large (Fig. 7a). For Posidonia shale our measured (opposing) effects of pressure and temperature on primary creep reveal that the P - T influence is of the same order as compositional changes. This is shown in Fig. 7a for simulated depths up to about 4 km (solid dots). For comparison, the orientation of the maximum principal stress with respect to bedding also has a distinct impact on the creep rate, where samples loaded parallel to bedding plane orientation are

p [21]

creeping at a lower rate compared to those deformed perpendicular to bedding (Fig. 7a, Tab. 4). The impact of water content on creep is also important as shown by Sone and Zoback (2014) for Haynesville shale dried at 100°C in comparison to as-is samples (Fig. 7a, Tab. 4). Enhanced creep rates for water saturated samples compared to dry samples of Eagle Ford shale were also recognized by Almasoodi et al. (2014) and for Callovo-Oxfordian argillite by Zhang and Rothfuchs (2004). Water may enhance creep rates in various ways, for example by capillary suction and osmotic swelling, poroelastic effects in saturated rocks or enhanced microcrack development in highly stressed clay-rich rocks (Nara et al., 2011; Schmitt et al., 1994; van Oort, 2003; Sone and Zoback, 2014). It should be recalled, however, that our calculated absolute values are biased by the choice of empirical flow law and used time interval for fitting as discussed above.

For a given shale formation, the amount of primary creep within 3 years increases with increasing fraction of weak phases (clays and kerogen) and decreasing proportion of carbonates (connected by broken lines in Fig. 7), as may be expected comparing the relative strength of the mineral and organic constituents. However, at least for carbonates, this conclusion is not valid if all data of all shown shales are considered. It should be noted that one calculated strain value for Haynesville (Hay4) is much higher than the others, which is associated with the unusual high m -value and low B -value determined by (Li and Ghassemi, 2012). In general, strain decreases with increasing fraction of strong (QFP) minerals, but not for single formations (broken lines in Fig. 7d). This increase of strain after 3 years deformation with larger fraction of strong minerals for individual formations seems counter-intuitive and may be explained only by the combined effect of all phases together on deformation as already noted for the short-term strength of shales (Rybacki et al., 2015). The same dataset is plotted in a ternary diagram of composition with superposed creep strain values given in % (Fig. 8a). Low strains, indicative for strong shales, are more common

towards the lower left corner of the diagram, i.e., for formations with high fraction of strong phases. For individual formations with approximately similar QFP-amount (connected by broken lines in Fig. 8a) the combined increase of weak phases and decrease of carbonates yields slightly increasing strains, but this effect is minor compared to the volumetric effect of strong minerals. This result suggests that the capacity of building a load bearing framework of strong minerals is important for the creep behavior of shales, at least at room temperature conditions.

The prospectivity of shales is often assumed to be linked to the so-called brittleness of rocks, where a number of different empirical definitions exist (Rybacki et al., 2016; Zhang et al., 2016a). As a first approximation, brittleness can be simply determined from composition if P - T effects are neglected. As shown by (Rybacki et al., 2016), in the brittle to semibrittle deformation regime at low depth ($\lesssim 4$ km), brittleness may be estimated from composition using the index:

$$B_{porocomp} = \frac{F_{QFP}}{F_{QFP} + 0.5F_{Cb} + F_{ClTOC} + \phi} \quad (12)$$

where F indicate volumetric fraction of constituents and ϕ is porosity. Brittle behavior is indicated by $B \rightarrow 1$ and ductile behavior by $B \rightarrow 0$. For B -values > 0.2 this brittleness index correlates rather well with deformation energy-based definitions (Rybacki et al., 2016). We calculated $B_{porocomp}$ (Tab. 4) and superposed the values in a similar ternary diagram (Fig. 8b). High brittleness correlates mainly with high amount of strong phases and less with the combined fraction of carbonates and weak phases, similar to creep strain. A (negative) correlation between strain and brittleness indicates that brittleness estimated from composition or short-term deformation experiments may be used to estimate the long-term fracture healing of shales (Figure 9). However, for individual shale formations (e.g., Eagle Ford and Haynesville in Fig. 9) this correlation is not clear.

4.4 Effect of Stress, Pressure and Temperature on Secondary Creep

The best fit of eqn. (9) to the secondary creep data yields large error bars. Irrespective of this, we find that the stress exponent $n_3 \approx 4.8$ (Tab. 3) clearly points to non-linear secondary creep. n -values between 3 and 5 are considered typical for high temperature dislocation creep of silicate rocks (Karato, 2008). Assuming stress corrosion to be rate-limiting, the stress exponent for brittle creep of hard rocks (granite, basalt, sandstone) was found to be between ≈ 7 and 19 (Brantut et al., 2012). However, the stress exponent resulting from a best fit to our data likely represents the stress sensitive of a transient interplay of several different micromechanisms. We are not aware of any other published steady state creep data on shales. Few data exist on creep behavior of Opalinus clay (Naumann et al., 2007), Boom clay (Yu et al., 2015) and Callovian-Oxfordian Bure Clay (Gasc-Barbier et al., 2004) and other argillaceous rocks (Fabre and Pellet, 2006; Zhang and Rothfuchs, 2004). These studies show that even under low differential stress (< 16 MPa) the apparent steady creep rate increases with stress nonlinearly. For Opalinus clay n is estimated close to 5 (Naumann et al., 2007). The appearance of a ‘steady state’ creep regime in this kind of rocks seems to depend on composition. For long time uniaxial creep tests lasting over hundreds of days, the creep rate tends to stabilize at about 10^{-11} - 10^{-10} s $^{-1}$, sometimes also associated with dilational behavior (Fabre and Pellet, 2006; Naumann et al., 2007; Yu et al. 2015; Zhang and Rothfuchs, 2004).

The temperature sensitivity of secondary creep with an activation energy Q_3 of about 74 kJ/mol is considerably higher than observed in the primary regime ($\approx 3 - 5$ kJ/mol). This may reflect a combination of the temperature sensitivity of creep of bitumen with Q between 114 and 175 kJ/mol (Mouazen et al., 2011) and of micas with $Q = 47 - 89$ kJ/mol (Ibanez and Kronenberg, 1993) which we assume similar to clays. For comparison, the activation energy for stress corrosion in granite and sandstone in the secondary regime is about 40 ± 10 kJ/mol

p [24]

(Brantut et al., 2012), which is less than our best fit value. The estimated activation volume $V_3 \approx -11 \text{ cm}^3/\text{mol}$ suggests that increasing pressure enhances shale creep rate which is counter-intuitive in the semibrittle deformation regime. However, the error bar of $167 \text{ cm}^3/\text{mol}$ is rather large, so that V_3 should be considered just as a best fit value. Note that the influence of V_3 on the creep rate is low compared to that of Q_3 , so that estimations of creep strains are still feasible.

Assuming that secondary creep can be activated at 30 MPa stress, the calculated strain after 3 years is between 0.25% at $T = 20^\circ$, $P = 20 \text{ MPa}$ and 217% at $T = 100^\circ$, $P = 100 \text{ MPa}$, respectively, which is considerably larger than in the primary regime (Tab. 4).

4.5 Effect of Creep on Fracture Healing

Healing of hydraulic fractures in shale formations may occur by several mechanisms. These include swelling of clay particles adjacent to the fracture by frac water penetration, chemical reaction between host rock and proppants in the presence of fluids leading to dissolution-precipitation processes, shear-enhanced fracture closure of non-propped fractures, creep of the host rock and embedment of proppants due to stress concentrations (e.g., Fisher et al., 2013). Here, we consider the impact of creep on proppant embedment and fracture healing.

After hydraulic fracturing time-dependent deformation of asperities on the fracture plane and the embedment of proppants may lead to closure of the fracture as implied by declining production rates. The healing process will be affected by elastic deformation, due to Hertzian contact forces or with progressive indentation by an empirical power law relationship (Chen et al., 2017). Inelastic creep will further lead to time-dependent proppant embedment possibly up to complete closure. Modelling of the complex stress distributions in such a scenario is beyond the scope of this study. For simplicity, we roughly estimate the creep-related healing

p [25]

by assuming that the proppants or asperities are composed of stiff cylindrical pillars between fracture faces with a diameter of $d = 0.3$ mm, typical for 40/70 mesh proppants. The indentation rate \dot{h} of these pillars into the shale matrix by creep may be estimated (Dorner et al., 2014):

$$\dot{h} = \dot{\epsilon} \cdot \frac{d}{c_2} \quad (13)$$

where the constant c_2 is 0.755 and $\dot{\epsilon}$ is the strain rate determined in conventional uniaxial creep experiments. The stress σ_{net} acting on the indenter is related to the corresponding uniaxial stress σ by $\sigma_{net} = \sigma / c_1$ with $c_1 = 0.296$. Integration of eqn. (13) and inserting eqns. (6) and (9) yields a proppant indentation depth h after time t of:

$$h_{pri} = \frac{d}{c_2} A_0 \sigma^{n_1} e^{-\left(\frac{Q_1 + P \cdot V_1}{R \cdot T}\right)} t^{m_0 \sigma^{n_2} \exp\left(-\frac{Q_2 + P \cdot V_2}{R \cdot T}\right)} \quad (14)$$

for primary creep and

$$h_{sec} = \frac{d}{c_2} B_0 \sigma^{n_3} e^{-\left(\frac{Q_3 + P \cdot V_3}{R \cdot T}\right)} t \quad (15)$$

for secondary creep, respectively.

Assuming one monolayer of proppants of fixed diameter covering the entire hydrofrac then the fracture will be closed if an indentation depth of $h = 0.15$ mm into both fracture surfaces is reached. We further assume that the net stress σ_{net} acting on the indenter is 30 MPa, corresponding to a uniaxial stress σ of about 10 MPa. For primary creep the time of complete closure is then between $1.4 \cdot 10^{29}$ and $2.2 \cdot 10^{25}$ years in a depth range between 2 km (with $P = 50$ MPa, $T = 50^\circ\text{C}$) and 4 km (with $P = 100$ MPa, $T = 100^\circ\text{C}$), respectively. Assuming instead a local stress concentration of $\sigma_{net} = 150$ MPa (i.e., $\sigma \approx 50$ MPa), the time reduces to $7.2 \cdot 10^{12}$ -

$2.4 \cdot 10^{10}$ years. Therefore, primary creep appears to be insufficient for fracture healing in-situ, where production rates strongly declines within several years. Repeating the calculation for secondary creep, we obtain for $\sigma_{net} = 30$ MPa closure times of 13.9 – 0.3 years in 2 - 4 km depth, i.e., much more realistic time intervals, and for $\sigma_{net} = 150$ MPa a duration of only between 2.2 days and 1.2 hours. This comparison suggests that fracture healing can be explained by creep-induced proppant embedment if local stress concentrations are sufficiently high so that long term creep rates do not decline significantly with time as would be deduced if only primary creep data are considered for extrapolation. Note, however, that these estimates assume constant stress on a cylindrical indenter and an initial fracture opening of only 0.3 mm. In addition, we ignored initial elastic indentation.

7. Conclusions

Creep experiments on Dotternhausen Posidonia shale at elevated pressure and temperature show the creep strain (rate) depend on the applied stress, temperature and pressure, indicative for semibrittle deformation. Most of the induced strain is accommodated by the weak phases (organic matter and phyllosilicates) and pore collapse. Dislocation activity in carbonate and strong minerals in minor and localized microcrack evolution only evident in samples deformed until failure.

At relatively low differential stress, samples showed primary creep with continuously decreasing creep rate. At higher stress we observed secondary and tertiary creep until final failure. To account for the stress, temperature and pressure dependence of strain (rate), we applied empirical power law creep equations in the primary and secondary creep regime. Estimation of the associated indentation rates of strong proppants into hydraulically fractured shale suggest that creep-induced healing may occur by local stress concentration that exceed

stresses leading to primary creep alone, even for the investigated relatively weak Dotternhausen shale.

To our knowledge, this is the first investigation of creep of shales at high pressure and temperature conditions. In the primary creep regime, a comparison of our results with published creep data of North American shales measured at ambient temperature indicates that the reservoir depth-related influence of pressure and temperature on long term creep strain is on the same order as the effect of changes in composition, bedding orientation, or variation in water content. The magnitude of creep strain is strongly influenced by the amount of strong minerals, allowing to form a load-bearing framework at high fraction. Therefore, the long term creep properties of shale may be correlated to composition-based brittleness at low depth.

Acknowledgements

This work was supported by the European Union's Horizon 2020 research and innovation programme under grant agreement No. 640979 (SXT). We thank Masline Makasi for sample handling, Stefan Gehrmann for sample and thin section preparation, Anja Schreiber for TEM foil preparation, Tobias Meier for providing porosity data and Michael Naumann for assistance with deformation experiments. Insightful comments of two anonymous reviewers improved the manuscript.

References

Akrad OM, Miskimins JL, Prasad M (2011) The effects of fracturing fluids on shale rock mechanical properties and proppant embedment. In: SPE annual technical conference and exhibition. Society of Petroleum Engineers, Denver

Almasoodi MM, Abousleiman YN, Hoang SK (2014) Viscoelastic creep of Eagle Ford shale: investigating fluid–shale interaction. In: SPE/CSUR Unconventional Resources Conference. Society of Petroleum Engineers, Calgary

Alramahi B, Sundberg MI (2012) Proppant embedment and conductivity of hydraulic fractures in shales. In: 46th U.S. Rock Mechanics/Geomechanics Symposium. American Rock Mechanics Association, Chicago

Atkinson BK, Meredith PG (1987) The theory of subcritical crack growth with applications to minerals and rocks. In: Atkinson BK (ed) Fracture mechanics of rock. Academic Press, London, pp 111–166

Baihly JD, Altman RM, Malpani R, Luo F (2010) Shale gas production decline trend comparison over time and basins. In: SPE annual technical conference and exhibition. Society of Petroleum Engineers, Florence

Bikong C, Hoxha D, Shao JF (2015) A micro-macro model for time-dependent behavior of clayey rocks due to anisotropic propagation of microcracks. *Int J Plast* 69:73–88

Bonini M, Debernardi D, Barla M, Barla G (2007) The mechanical behaviour of clay shales and implications on the design of tunnels. *Rock Mech Rock Eng* 42:361

Brantut N, Baud P, Heap MJ, Meredith PG (2012) Micromechanics of brittle creep in rocks. *J Geophys Res* 117:B08412

Brantut N, Heap MJ, Meredith PG, Baud P (2013) Time-dependent cracking and brittle creep in crustal rocks: a review. *J Struct Geol* 52:17–43

Brantut N, Heap MJ, Baud P, Meredith PG (2014) Rate- and strain-dependent brittle deformation of rocks. *J Geophys Res Solid Earth* 119:1818–1836

Bürgmann R, Dresen G (2008) Rheology of the lower crust and upper mantle: evidence from rock mechanics, geodesy, and field observations. *Annu Rev Earth Planet Sci* 36:531–567

Chang C, Zoback MD (2009) Viscous creep in room-dried unconsolidated Gulf of Mexico shale (I): experimental results. *J Pet Sci Eng* 69:239–246

Chang C, Zoback MD (2010) Viscous creep in room-dried unconsolidated Gulf of Mexico shale (II): development of a viscoplasticity model. *J Pet Sci Eng* 72:50–55

Chen D, Ye Z, Pan Z, Zhou Y, Zhang J (2017) A permeability model for the hydraulic fracture filled with proppant packs under combined effect of compaction and embedment. *J Pet Sci Eng* 149:428–435

Chong KP, Smith JW, Khaliki BA (1978) Creep and relaxation of oil shale. In: 19th U.S. Symposium on Rock Mechanics (USRMS). American Rock Mechanics Association, Reno

Ciccotti M (2009) Stress-corrosion mechanisms in silicate glasse. *J Phys D Appl Phys* 42:214006. doi:10.1088/0022-3727/42/21/214006

Cogan J (1976) Triaxial creep tests of Opohonga limestone and Ophir shale. *Int J Rock Mech Min Sci Geomech Abstr* 13:1–10

de Waal JA, Smits RMM (1988) Prediction of reservoir compaction and surface subsidence: field application of a new model. *SPE Form Eval* 3:347–356

Dorner D, Röller K, Stöckhert B (2014) High temperature indentation creep tests on anhydrite—a promising first look. *Solid Earth* 5:805–819

Dudley JW II, Myers MT, Shew RD, Arasteh MM (1998) Measuring compaction and compressibilities in unconsolidated reservoir materials by time-scaling creep. *SPE Reservoir Eval Eng* 1:430–437

Fabre G, Pellet F (2006) Creep and time-dependent damage in argillaceous rocks. *Int J Rock Mech Min Sci* 43:950–960

Findley WN, Lai JS, Onaran K (1976) Creep and relaxation of nonlinear viscoelastic materials with an introduction to linear viscoelasticity. Dover Publications, New York

Fischer Q, Kets F, Crook A (2013) Self-sealing of faults and fractures in argillaceous formations: evidence from the petroleum industry. *Nagra Arbeitsber. NAB* 13-06

Fjær E, Larsen I, Holt RM, Bauer A (2014) A creepy model for creep. In: 48th U.S. Rock Mechanics/Geomechanics Symposium. American Rock Mechanics Association, Minneapolis

Frost H, Ashby M (1982) Deformation-mechanism maps. The plasticity and creep of metals and ceramics. Pergamon Press, Oxford

Gasc-Barbier M, Chanchole S, Bérest P (2004) Creep behavior of Bure clayey rock. *Appl Clay Sci* 26:449–458

Guo J, Liu Y (2012) Modeling of proppant embedment: elastic deformation and creep deformation. In: SPE international production and operations conference & exhibition. Society of Petroleum Engineers, Doha

Gupta VB (1975) The creep behavior of standard linear solid. *J Appl Polym Sci* 19:2917

Hagin P, Zoback M (2004) Viscous deformation of unconsolidated reservoir sands—Part 2: linear viscoelastic models. *Geophysics* 69:742–751

Hart E (1970) A phenomenological theory for plastic deformation of polycrystalline metals. *Acta Metall* 18:599–610

Heap MJ, Baud P, Meredith PG, Bell AF, Main IG (2009a) Time-dependent brittle creep in Darley Dale sandstone. *J Geophys Res Solid Earth* 114:B07203

Heap MJ, Baud P, Meredith PG (2009b) Influence of temperature on brittle creep in sandstones. *Geophys Res Lett* 36:L19305. doi:10.1029/2009GL039373

Heller RJ, Zoback MD (2011) Adsorption, swelling and viscous creep of synthetic clay samples. In: 45th U.S. Rock Mechanics/Geomechanics Symposium. American Rock Mechanics Association, San Francisco

Hol S, Zoback MD (2013) Creep behavior of coal and shale related to adsorption of reservoir fluids. In: 47th U.S. Rock Mechanics/Geomechanics Symposium. American Rock Mechanics Association, San Francisco

Howarth RW, Ingraffea A, Engelder T (2011) Natural gas: should fracking stop? *Nature* 477:271–275

Hughes JD (2013) Energy: a reality check on the shale revolution. *Nature* 494:307–308

Ibanez WD, Kronenberg AK (1993) Experimental deformation of shale: mechanical properties and microstructural indicators of mechanisms. *Int J Rock Mech Min Sci Geomech Abstr* 30:723–734

Jiang Q, Qi Y, Wang Z, Zhou C (2013) An extended Nishihara model for the description of three stages of sandstone creep. *Geophys J Int* 193:841–854

Karato S (2008) Deformation of earth materials. Cambridge University Press, New York

Kassis SM, Sondergeld CH (2010) Gas shale permeability: effects of roughness, proppant, fracture offset, and confining pressure. In: International oil and gas conference and exhibition in China. Society of Petroleum Engineers, Beijing

Kranz RL (1980) The effects of confining pressure and stress difference on static fatigue of granite. *J Geophys Res* 85(B4):1854–1866

Kranz RL, Harries WJ, Carter NL (1982) Static fatigue of granite at 200°C. *Geophys Res Lett* 9:1–4

LaFollette RF, Carman PS (2010) Proppant diagenesis: results so far. In: SPE Unconventional Gas Conference. Society of Petroleum Engineers, Pittsburgh

Li Y, Ghassemi A (2012) Creep behavior of Barnett, Haynesville, and Marcellus shale. In: 46th U.S. Rock Mechanics/Geomechanics Symposium. American Rock Mechanics Association, Chicago

Li X, Shao Z (2016) Investigation of macroscopic brittle creep failure caused by microcrack growth under step loading and unloading in rocks. *Rock Mech Rock Eng* 49:2581–2593

Liu Y, Sharma MM (2005) Effect of fracture width and fluid rheology on proppant settling and retardation: an experimental study. In: SPE annual technical conference and exhibition. Society of Petroleum Engineers, Dallas

Lockner DA (1995) Rock Failure. In: Ahrens TJ (ed) *Rock physics and phase relations: a handbook of physical constants*. Ref. Shelf. AGU, Washington, pp 127–147

Main IG (2000) A damage mechanics model for power-law creep and earthquake aftershock and foreshock sequences. *Geophys J Int* 142:151–161

Masuti S, Barbot SD, Karato S-I, Feng L, Banerjee P (2016) Upper-mantle water stratification inferred from observations of the 2012 Indian Ocean earthquake. *Nature* 538:373–377

McGlade C, Speirs J, Sorrell S (2013) Unconventional gas—a review of regional and global resource estimates. *Energy* 55:571–584

Mighani S, Taneja S, Sondergeld CH, Rai CS (2015) Nanoindentation creep measurements on shale. In: 49th U.S. Rock Mechanics/Geomechanics Symposium. American Rock Mechanics Association, San Francisco

Morales RH, Suarez-Rivera R, Edelman E (2011) Experimental evaluation of hydraulic fracture impairment in shale reservoirs. In: 45th U.S. Rock Mechanics/Geomechanics Symposium. American Rock Mechanics Association, San Francisco

Mouazen M, Poulesquen A, Vergnes B (2011) Correlation between thermal and rheological studies to characterize the behavior of bitumen. *Rheol Acta* 50:169–178

Naumann M, Hunsche U, Schulze O (2007) Experimental investigations on anisotropy in dilatancy, failure and creep of Opalinus Clay. *Phys Chem Earth Parts A/B/C* 32:889–895

Norris JQ, Turcotte DL, Moores EM, Brodsky EE, Rundle JB (2016) Fracking in Tight Shales: what is it, what does it accomplish, and what are its consequences? *Annu Rev Earth Planet Sci* 44:321–351

Paterson MS (1970) A high-pressure, high-temperature apparatus for rock deformation. *Int J Rock Mech Min Sci* 7:517–526

Paterson M (2013) *Materials science for structural geology*. Springer, London

Paterson MS, Wong TF (2005) *Experimental rock deformation—the brittle field*, 2nd edn. Springer, Berlin

Patzek T, Male F, Marder M (2014) A simple model of gas production from hydrofractured horizontal wells in shales. AAPG Bull 98:2507–2529

Pedlow J, Sharma M (2014) Changes in shale fracture conductivity due to interactions with waterbased fluids. In: SPE hydraulic fracturing technology conference. Society of Petroleum Engineers, The Woodlands

Ranalli G (1987) Rheology of the earth: deformation and flow processes in geophysics and geodynamics. Allen & Unwin, Boston

Rassouli FS, Zoback MD (2015) Long-term creep experiments on Haynesville shale rocks. In: 49th U.S. Rock Mechanics/Geomechanics Symposium. American Rock Mechanics Association, San Francisco

Reinicke A, Rybacki E, Stanchits S, Huenges E, Dresen G (2010) Hydraulic fracturing stimulation techniques and formation damage mechanisms—implications from laboratory testing of tight sandstone–proppant systems. Chemie der Erde - Geochemistry 70(Supplement 3):107–117

Rybacki E, Paterson MS, Wirth R, Dresen G (2003) Rheology of calcite–quartz aggregates deformed to large strain in torsion. J Geophys Res 108:2089. doi:10.1029/2002JB001833

Rybacki E, Reinicke A, Meier T, Makasi M, Dresen G (2015) What controls the mechanical properties of shale rocks?—Part I: strength and Young’s modulus. J Pet Sci Eng 135:702–722

Rybacki E, Meier T, Dresen G (2016) What controls the mechanical properties of shale rocks?— Part II: brittleness. J Pet Sci Eng 144:39–58

Schmitt L, Forsans T, Santarelli FJ (1994) Shale testing and capillary phenomena. Int J Rock Mech Min Sci 31:441–447

Sone H, Zoback MD (2010) Strength, creep and frictional properties of gas shale reservoir rocks. In: 44th U.S. Rock Mechanics Symposium and 5th U.S.-Canada Rock Mechanics Symposium. American Rock Mechanics Association, Salt Lake City

Sone H, Zoback MD (2011) Visco-plastic properties of shale gas reservoir rocks. In: 45th U.S. Rock Mechanics/Geomechanics Symposium. American Rock Mechanics Association, San Francisco

Sone H, Zoback MD (2013) Mechanical properties of shale-gas reservoir rocks—Part 2: ductile creep, brittle strength, and their relation to the elastic modulus. *Geophysics* 78:D393–D402

Sone H, Zoback MD (2014) Time-dependent deformation of shale gas reservoir rocks and its longterm effect on the in situ state of stress. *Int J Rock Mech Min Sci* 69:120–132

Stegent NA, Wagner AL, Mullen J, Borstmayer RE (2010) Engineering a successful fracture stimulation treatment in the Eagle Ford shale. In: Tight Gas Completions Conference. Society of Petroleum Engineers, San Antonio

Stouffer DC, Dame LT (1996) Inelastic deformation of metals. Wiley, New York

van Oort E (2003) On the physical and chemical stability of shales. *J Pet Sci Eng* 38:213–235

Volk LJ, Raible CJ, Carroll HB, Spears JS (1981) Embedment of high strength proppant into lowpermeability reservoir rock. In: SPE/DOE low permeability gas reservoirs symposium. Society of Petroleum Engineers, Denver

Wang H (2016) What factors control shale gas production decline trend: a comprehensive analysis and investigation. In: SPE/IAEE hydrocarbon economics and evaluation symposium. Society of Petroleum Engineers, Houston

Wilshire B, Burt H (2008) Damage evolution during creep of steels. *Int J Press Vessels Pip* 85:47–54

Yang Y, Zoback M (2016) Viscoplastic deformation of the Bakken and adjacent formations and its relation to hydraulic fracture growth. *Rock Mech Rock Eng* 49:689–698

Yu HD, Chen WZ, Gong Z, Tan XJ, Ma YS, Li XL, Sillen X (2015) Creep behavior of boom clay. *Int J Rock Mech Min Sci* 76:256–264

Zhang C, Rothfuchs T (2004) Experimental study of the hydro-mechanical behaviour of the Callovo-Oxfordian argillite. *Appl Clay Sci* 26:325–336

Zhang J, Kamenov A, Zhu D, Hill D (2013) Laboratory measurement of hydraulic fracture conductivities in the Barnett Shale. In: *International Petroleum Technology Conference*. International Petroleum Technology Conference, Beijing

Zhang J, Ouyang L, Zhu D, Hill AD (2015) Experimental and numerical studies of reduced fracture conductivity due to proppant embedment in the shale reservoir. *J Pet Sci Eng* 130:37–45

Zhang D, Ranjith PG, Perera MSA (2016a) The brittleness indices used in rock mechanics and their application in shale hydraulic fracturing: a review. *J Pet Sci Eng* 143:158–170

Zhang J, Zhu D, Hill AD (2016b) Water-induced damage to propped-fracture conductivity in shale formations. *SPE Prod Oper* 31:147–156

Tab. 1: Experimental conditions

sample	P	T	σ	t_{\max}	ϵ_{\max}	m	A	$\dot{\epsilon}_{\min}$	rem
	MPa	°C	MPa	s	-	-	s^{-m}	s^{-1}	
DOT01	50	100	166	4100	0.1			$6.5 \cdot 10^{-6}$	failure
DOT02	50	100	150	168000	0.06	0.0659	0.02553		
DOT03	50	100	157	2400	0.1			$1.1 \cdot 10^{-5}$	failure
DOT04	50	100	148	595000	0.07	0.06474	0.02738		
DOT05	50	50	157	97000	0.09			$2.4 \cdot 10^{-7}$	failure
DOT06	50	150	127	430	0.12			$8.8 \cdot 10^{-5}$	failure
DOT07	50	75	160	500	0.09			$5.8 \cdot 10^{-5}$	failure
DOT08	75	100	164	60	0.18			$2.6 \cdot 10^{-3}$	failure
DOT09	100	100	169	1500	0.20			$4.2 \cdot 10^{-5}$	failure
DOT10	200	100	200	610	0.26			$1.2 \cdot 10^{-4}$	failure
DOT11	75	100	155	70	0.16			$2.0 \cdot 10^{-3}$	failure
DOT12	150	100	205	10700	0.13	0.07479	0.06242		
DOT101	100	100	111	79000	0.04	0.07408	0.01461		
DOT103	100	100	152	4700	0.06	0.08448	0.02383		
DOT104	50	100	154	900	0.06	0.10740	0.02420		
DOT105	150	100	154	22000	0.05	0.04628	0.02349		
DOT107	100	200	113	5100	0.05	0.08024	0.02006		
DOT108	100	200	61	26000	0.03	0.09907	0.00841		
DOT109	50	50	156	25000	0.04	0.05044	0.02188		
DOT110	100	50	110	154000	0.03	0.04583	0.01472		

Tab. 2: Primary creep fit parameter for sample DOT04

creep law	parameter for time-interval	22 – 595395 s (\approx 1 week)	50 – 5000 s (\approx 1.4 h)
parabolic	A	0.02340	0.02738
	m	0.08117	0.06474
	r_{fit}^2	0.99858	0.99972
	strain after 3 years	0.104 (92.9%)	0.090 (80.4%)
logarithmic	A	0.00514	0.0237
	B	0.01096	0.00641
	r_{fit}^2	0.98809	0.99861
	strain after 3 years	0.093 (83.0%)	0.075 (67.0%)
exponential	A	0.06847	0.0474
	B	0.01843	0.00984
	t_0	1.58263×10^5	1.4184×10^3
	r_{fit}^2	0.97169	0.97841
	strain after 3 years	0.069 (61.6%)	0.074 (66.1%)
hyperbolic	A	0.0217	0.2374
	B	2.82	2.24×10^{-15}
	s	0.0438	0.0640
	r_{fit}^2	0.99909	0.99971
	strain after 3 years	0.112 (100%)	0.091 (88.4%)
crack-damage	A	530.15	2.84
	B	1018.30	270.96
	k	4.336×10^{42}	1.141×10^{25}
	r_{fit}^2	0.99737	0.99954
	strain after 3 years	0.101 (90.2%)	0.085 (72.3%)

Tab. 3: Parameters for stress, temperature and pressure dependence of primary and secondary creep

parameter	primary creep	secondary creep
n_1	1.37 ± 0.10	
n_2	$\equiv 0$	
n_3		4.8 ± 18.3
Q_1	$2.54 \pm 0.76 \text{ kJmol}^{-1}$	
Q_2	$4.79 \pm 1.86 \text{ kJmol}^{-1}$	
Q_3		$73.8 \pm 56.4 \text{ kJmol}^{-1}$
V_1	$0.92 \pm 0.92 \text{ cm}^3 \text{mol}^{-1}$	
V_2	$11.14 \pm 6.84 \text{ cm}^3 \text{mol}^{-1}$	
V_3		$-11.3 \pm 167.2 \text{ cm}^3 \text{mol}^{-1}$
A_0	$(5.62 \pm 0.46) \cdot 10^{-5} \text{ MPa}^{-1.37} \text{ s}^{-m}$	
m_0	0.43 ± 0.26	
B_0		$(2.8 \pm 224) \cdot 10^{-5} \text{ MPa}^{-4.8} \text{ s}^{-1}$

Tab. 4: Primary creep strain of various shales

shale	poro, vol%	QFP, vol%	Cb, vol%	ClyTOC, vol%	B _T MPa ^{-m}	B _{II} MPa ^{-m}	m _T	m _{II}	ε _T %	ε _{II} %	ε _{T-dry} %	ε _T %	ε _T %	ε _T %	B _{porocomp}
T, °C	-	-	-	-	20	20	20	20	20	20	20	50	75	100	-
P, MPa	-	-	-	-	20	20	20	20	20	20	20	50	75	100	-
Pos ^a	11	14	42	33	2.0·10 ⁻⁵		0.05		0.57			0.67	0.75	0.82	0.18
Bar1 ^b	5	51	2	42	4.0·10 ⁻⁵	2.3·10 ⁻⁵	0.02	0.016	0.17	0.09					0.52
Bar2 ^b	1	41	52	6	1.5·10 ⁻⁵	1.4·10 ⁻⁵	0.017	0.01	0.06	0.05					0.55
Bar3 ^c		60	10	30	4.5·10 ⁻⁸		0.35		0.08						0.63
Hay1 ^b	6	33	21	40	5.0·10 ⁻⁵	2.1·10 ⁻⁵	0.05	0.038	0.38	0.13	0.27				0.37
Hay2 ^b	3	23	51	23	2.2·10 ⁻⁵	1.7·10 ⁻⁵	0.037	0.025	0.13	0.08					0.31
Hay3 ^d		27	8	65	4.5·10 ⁻⁵	2.3·10 ⁻⁵	0.055	0.018	0.37	0.09					0.28
Hay4 ^c		25	23	51	1.0·10 ⁻⁷		0.47		1.78						0.29
Eag1 ^b	6	24	50	20	5.0·10 ⁻⁵	2.0·10 ⁻⁵	0.058	0.04	0.44	0.13					0.32
Eag2 ^b	6	15	71	8	3.8·10 ⁻⁵	1.8·10 ⁻⁵	0.058	0.038	0.33	0.11					0.23
Mar1 ^c		28	9	64	2.6·10 ⁻⁷		0.35		0.48						0.29

poro= porosity, QFP = quartz+feldspar+pyrite, Cb = carbonates, ClyTOC = clays + organic matter, B and m = power law parameter for primary creep (cf., eqn.

(11)), ε = creep strain after 3 years at σ = 30 MPa and P-T conditions indicated, B_{porocomp} = brittleness index; subscripts T and II refer to loading perpendicular and parallel to bedding, respectively, dry = dried at 100°C; Pos = posidonia, Bar = Barnett, Hay = Haynesville, Eag = Eagle Ford, Mar = Marcellus; superscript a = this work, b = Sone and Zoback (2014), c = Li and Ghassemi (2012), d = Rassouli and Zoback (2015).

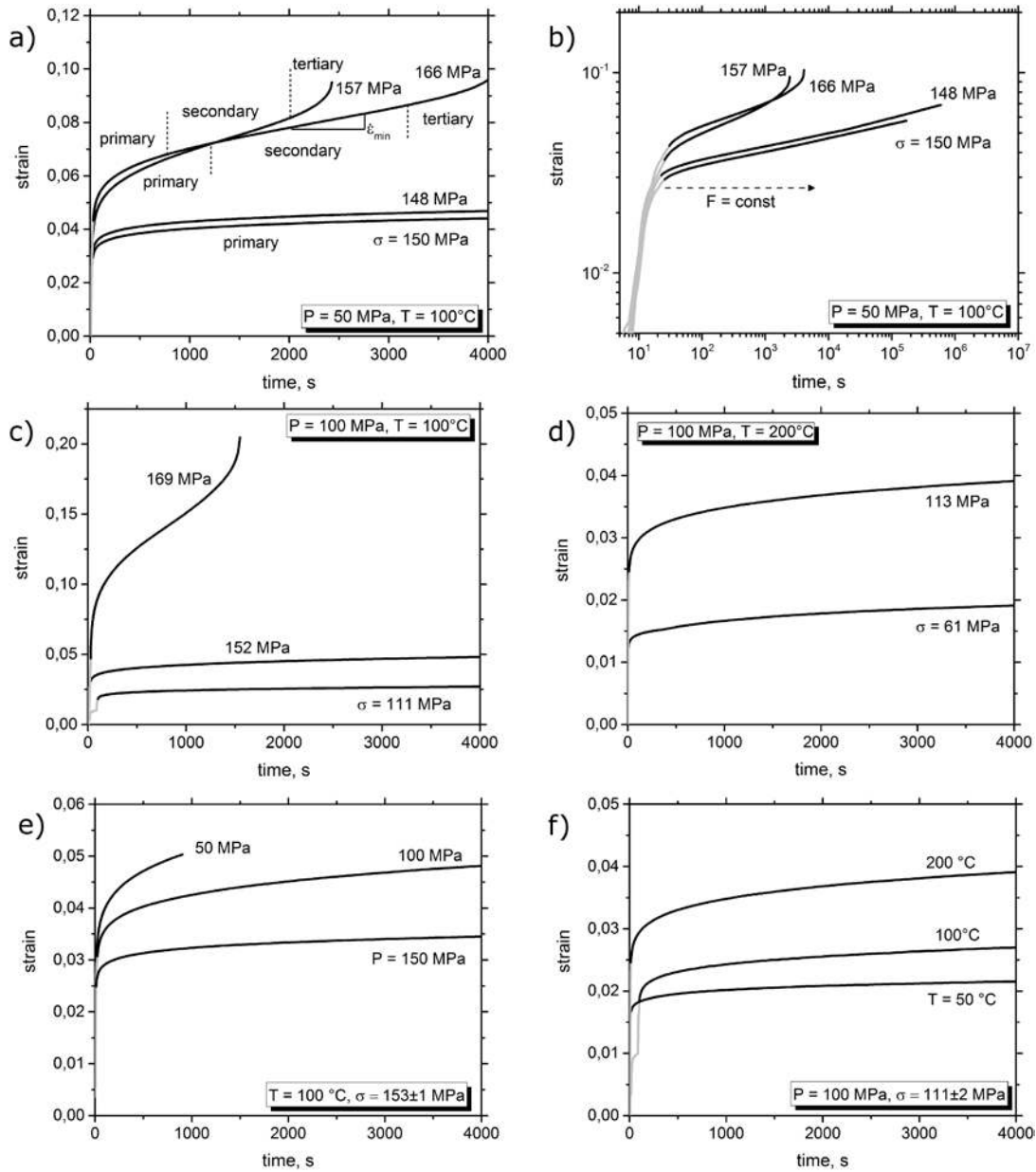


Figure 1: Creep curves of Dotternhausen Posidonia shale in relation to applied differential stress σ (a-d), confining pressure P (e) and temperature T (f). At high stress, creep curves show not only primary (decelerating), but also secondary (quasi steady state) and tertiary (accelerating) creep leading to final failure. Increasing pressure reduces the creep rate (e), whereas increasing temperature enhances the creep rate (f). For comparison, all curves are cut off at 4000 s except in (b), where complete curves are shown in log-log scale. During the first few sec the applied force F was increased up to the desired level that stabilized within 10-20 sec and subsequently held constant until manual test termination or sample failure (b).

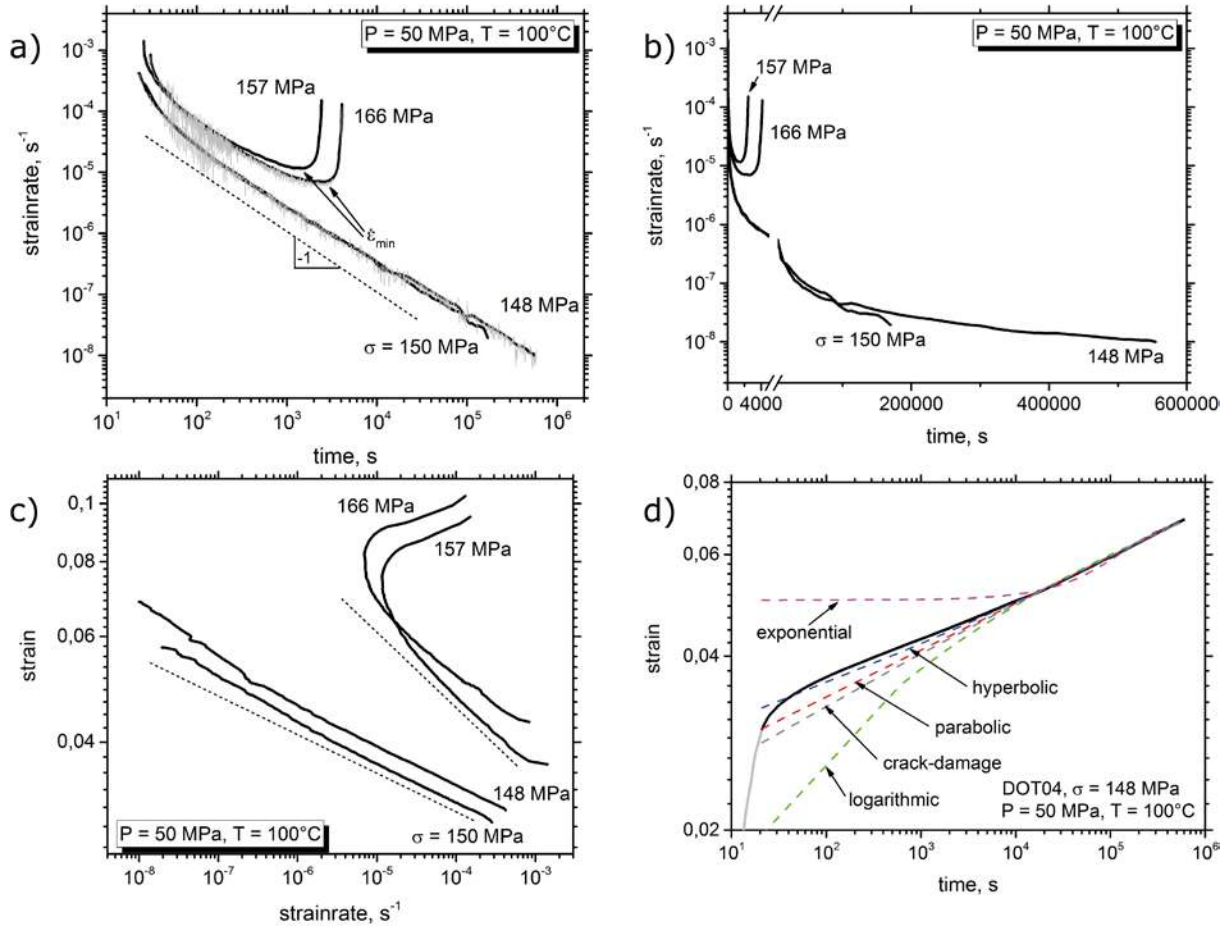


Figure 2: Creep curves of Posidonia shale deformed at 50 MPa pressure and 100°C temperature, scaled in (a) log(strain rate) versus log(time), (b) log(strain rate) vs time and (c) log(strain) vs log(strain rate). In (a) two unsmoothed curves are shown in light grey. For primary creep at low stress, the strain rate decreased continuously with increasing time (a, b) or strain (c). Minimum strain rates for secondary creep of high stress samples are indicated in (a). Dashed lines in (a) and (c) indicate linear relationships between strain rate and time or strain in log-log scale, respectively. Note the break of time-scale in (b). Fitted curves for primary creep of sample DOT04 ($\sigma = 148$ MPa) using different creep laws are shown in (d) in log(strain) vs log(time) scale. See text for details.

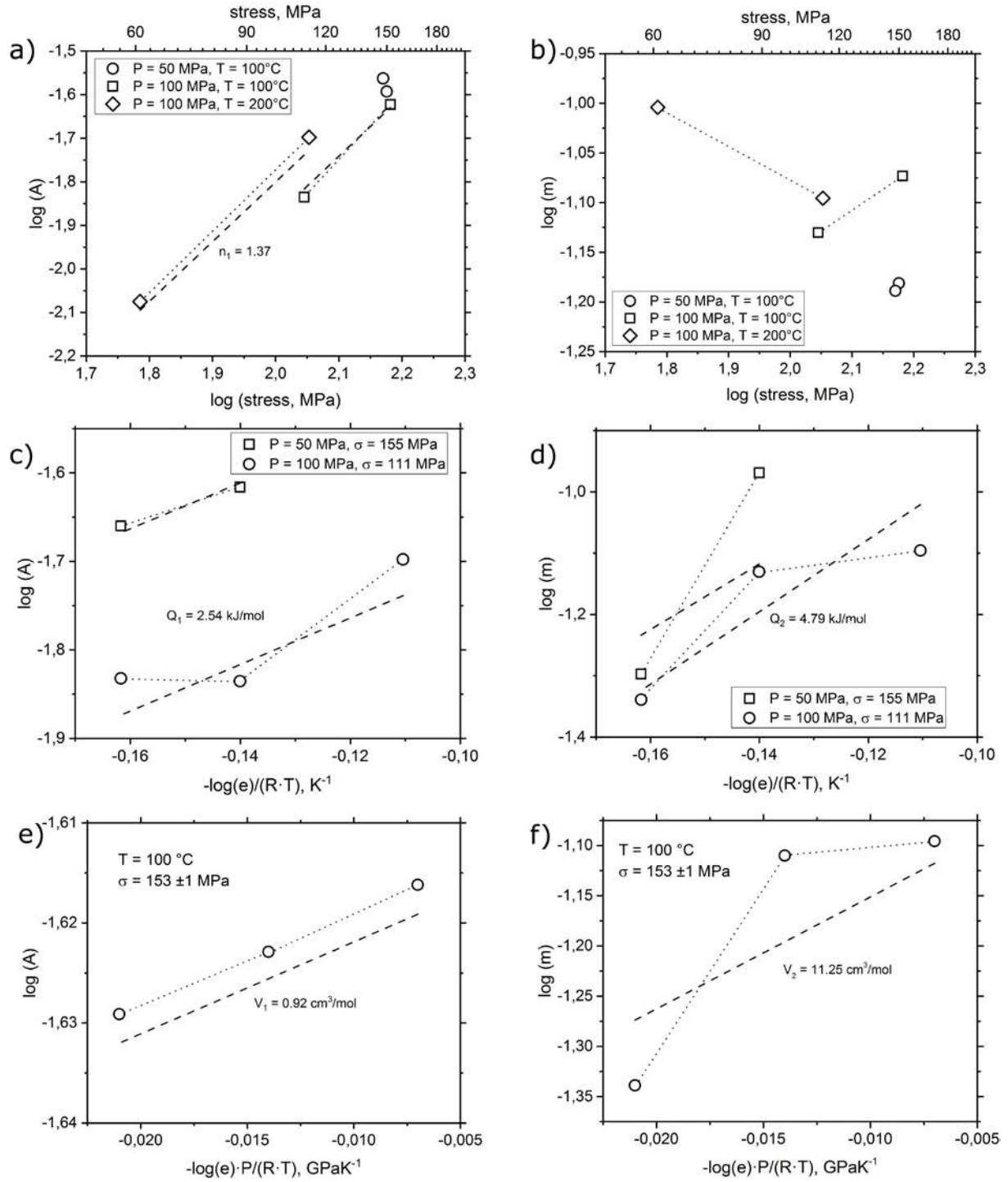


Figure 3: Variation of transient power law creep parameters A and m (cf., eqns. 1, 6) with differential stress (a, b), temperature (c, d) and pressure (e, f). Deformation conditions are indicated. Broken lines show multiple regression fits for stress sensitivity (n), activation energy (Q) and activation volume (V) of A (subscript 1) and m (subscript 2), respectively.

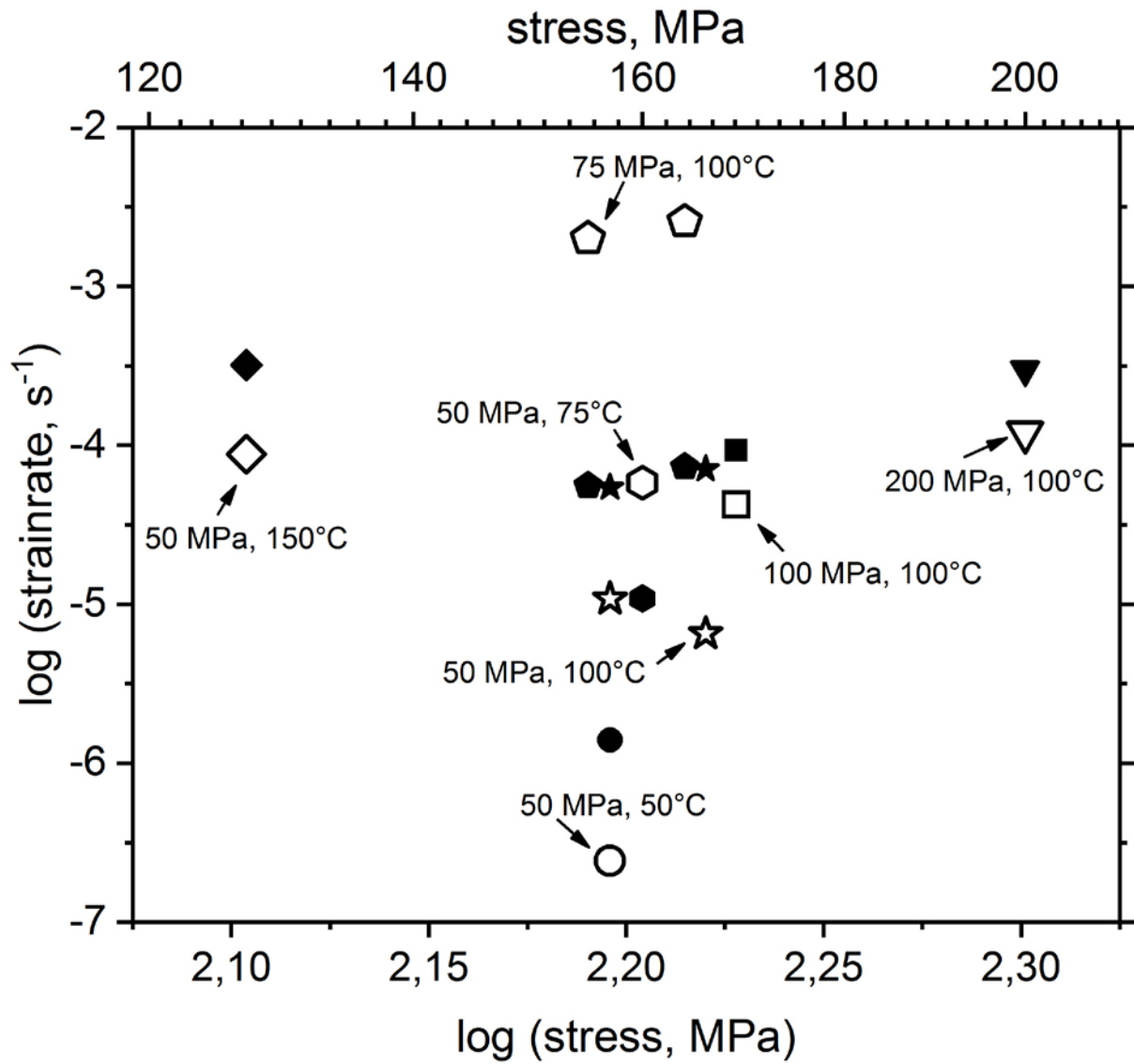


Figure 4: Measured (open symbols) and fitted (solid symbols) minimum creep strain rates of high stress samples versus applied stress. Pressure, temperature conditions are labelled.

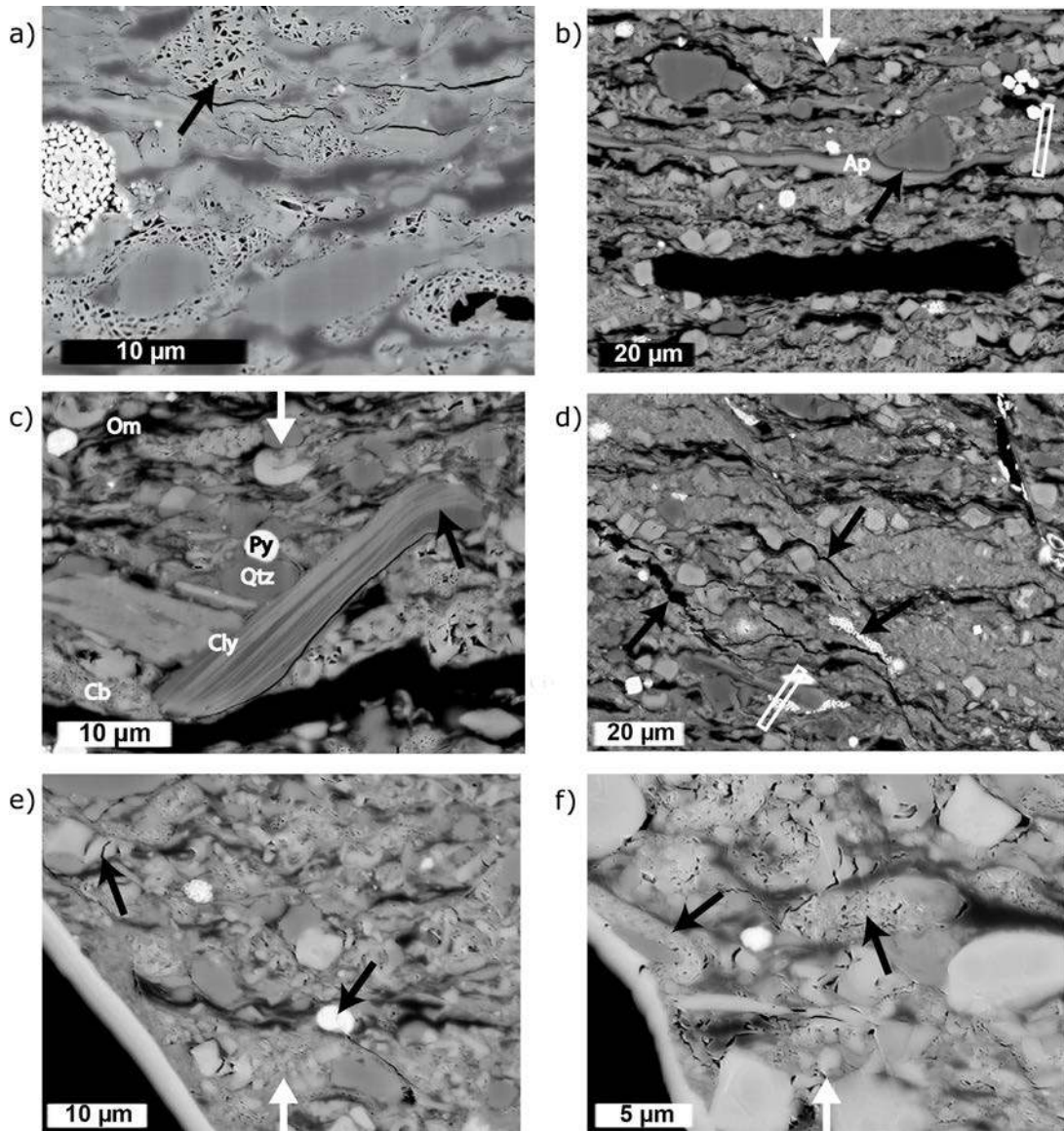


Figure 5: SEM-BSE images of undeformed (a) and deformed (b-f) Posidonia shale samples. White arrows indicate (vertical) loading direction. Main constituents are carbonates (Cb), clays (Cly), organic matter (Om), quartz (Qtz) and pyrite (Py), c.f., (c). Ap is apatite (b). Porosity is about 11% (black arrow in a). Low stress sample DOT04 was deformed by primary creep, showing indentation of strong partictes (Qtz) into the weaker matrix (arrow in b) and bending of phyllosilicates (arrow in c). High stress sample DOT07, formed until failure, reveals in addition formation of intercrystalline microcracks (arrows in d) oriented subparallel to the macrocrack (bottom left black area in e and f), intracrystalline cracks (arrows in e) and pore collapse adjacent to the macrocrack (arrows in f). Note that subhorizontal cracks are related to unloading. The white rectangles in (b) and (d) indicate the positions of FIB foils used for TEM (cf., Fig. 6).

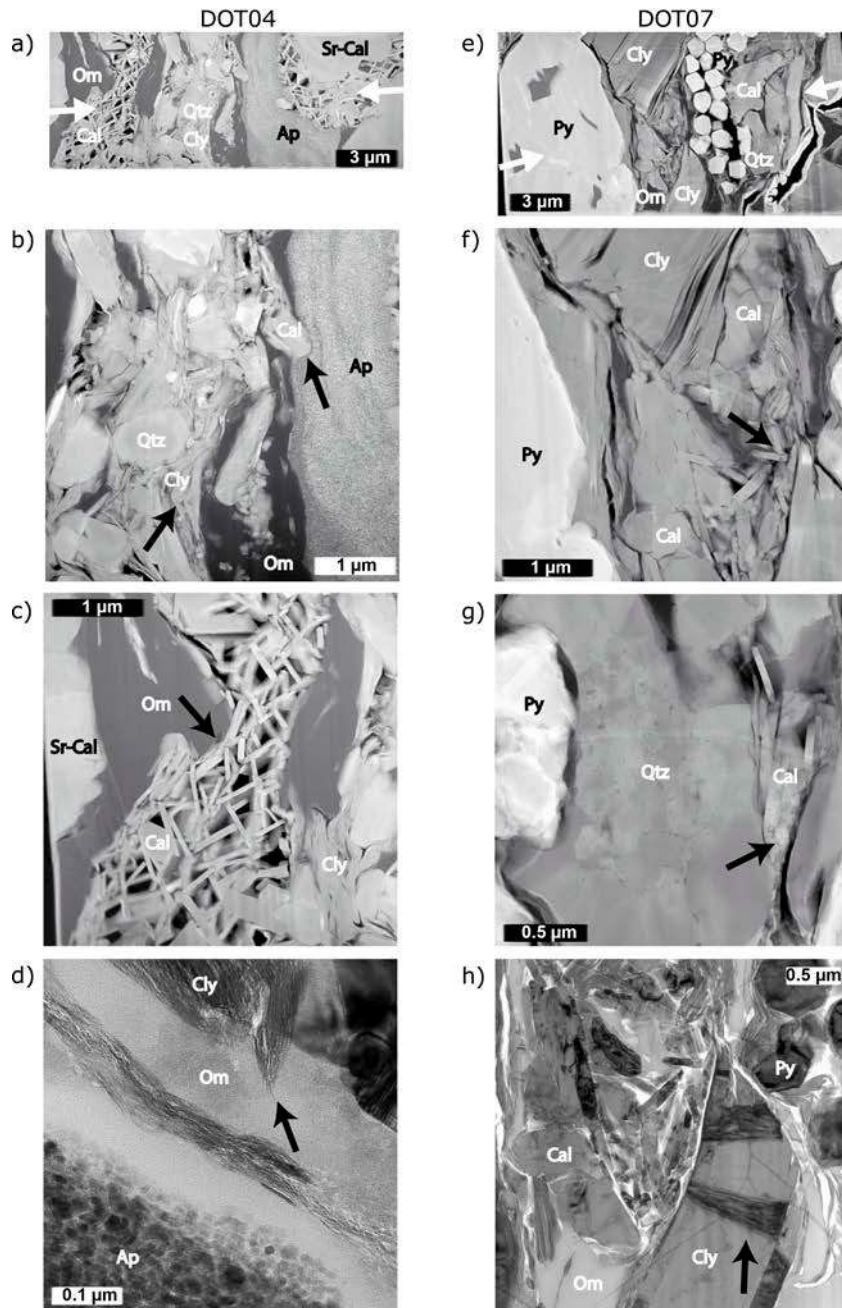


Figure 6: TEM micrographs of deformed low stress sample DOT04 (a-d) and high stress sample DOT07 (e-f). White arrows in overview images (a) and (f) indicate (subhorizontal) loading direction. For mineral abbreviations see Fig. 5. Cal is pure calcite and Sr-Cal is Sr-bearing calcite. In some places, the pore space between calcite flakes is reduced normal to the loading direction (black arrows in c and f). Calcite flakes are crushed if squeezed between strong neighboring grains (arrow in g) and embeds apatite (right arrow in b), which is composed of abundant small grains (bottom left in d). Clays around strong particles are bent (left arrow in b, arrow in h) and embed the organic matter (arrow in d). Bright field images (d, h) show almost no dislocations within all minerals.

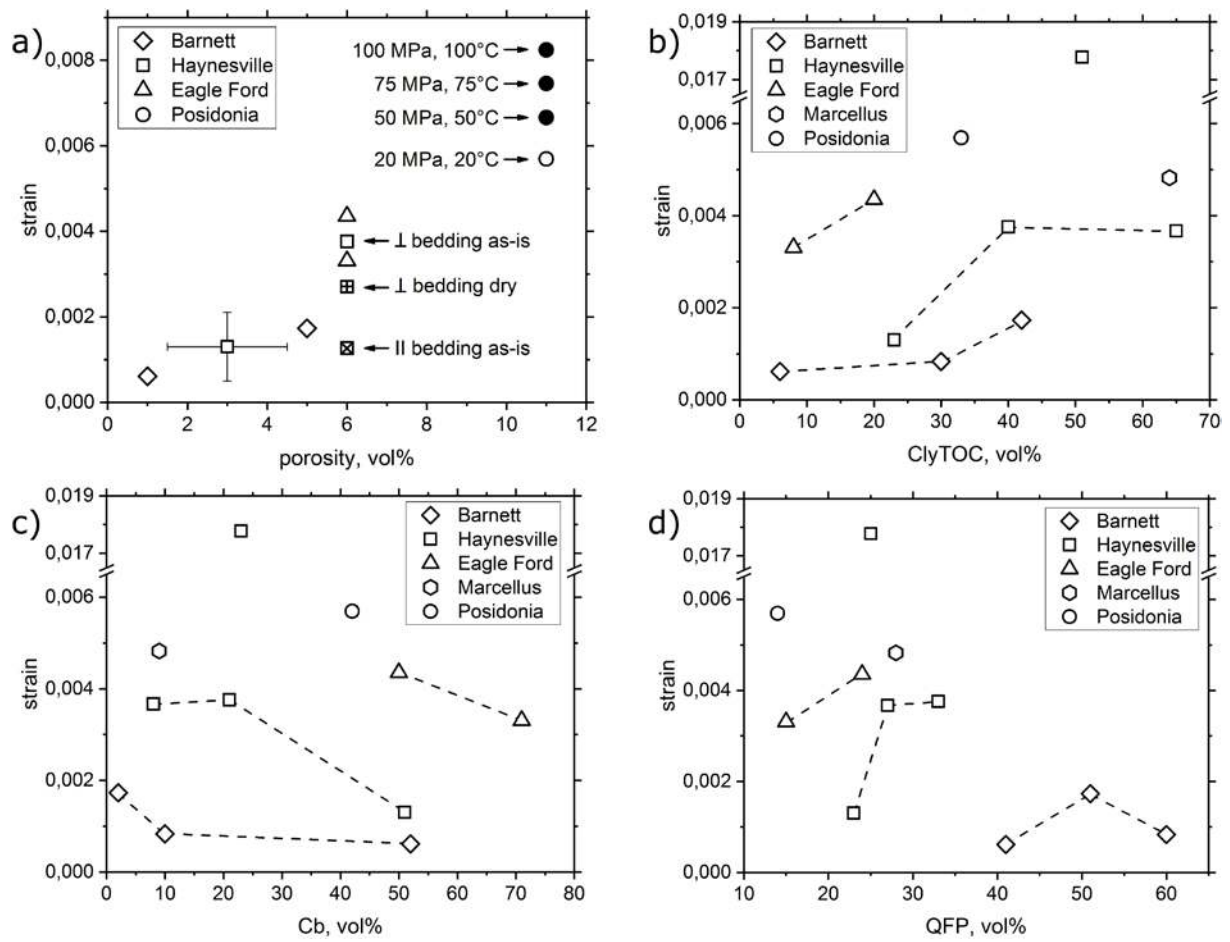


Figure 7: Calculated creep strain for primary creep of various shales after 3 years at 30 MPa stress versus porosity (a), fraction of clays and organic matter (b), carbonate content (c) and amount of quartz + feldspar + pyrite (d). Open symbols denote estimated strain at a pressure of 20 MPa and temperature of 20°C for shales with as-is water content, deformed perpendicular to bedding. Solid dots are calculated strains for Posidonia shale at elevated temperatures and pressures simulating depth of 2, 3 and 4 km assuming a geothermal gradient of 25°C/km and overburden of 25 MPa/km, respectively. Centered squares show the effect of drying and bedding-parallel (II) deformation on creep of Haynesville shale. Data of American shales are mean values estimated from data published Sone and Zoback (2014), Li and Ghassemi (2012), and Rassouli and Zoback (2015).

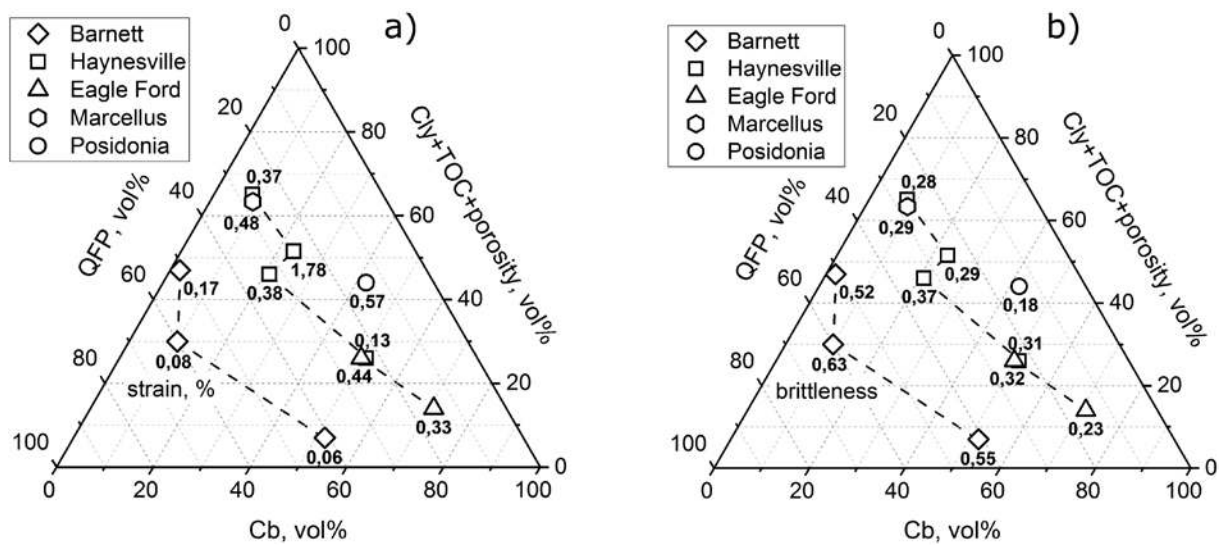


Figure 8: Creep strain (in %) after 3 years deformation at 30 MPa stress and 20°C temperature, 20 MPa pressure (a) and brittleness ($B_{porocomp}$) determined from composition (b) plotted in ternary diagrams with fraction of mechanically weak phases (clay, organics, pores), strong phases (QFP = quartz + feldspar + pyrite) and intermediate strong carbonates (Cb). Data of American shales are mean values estimated from data published Sone and Zoback (2014), Li and Ghassemi (2012), and Rassouli and Zoback (2015).

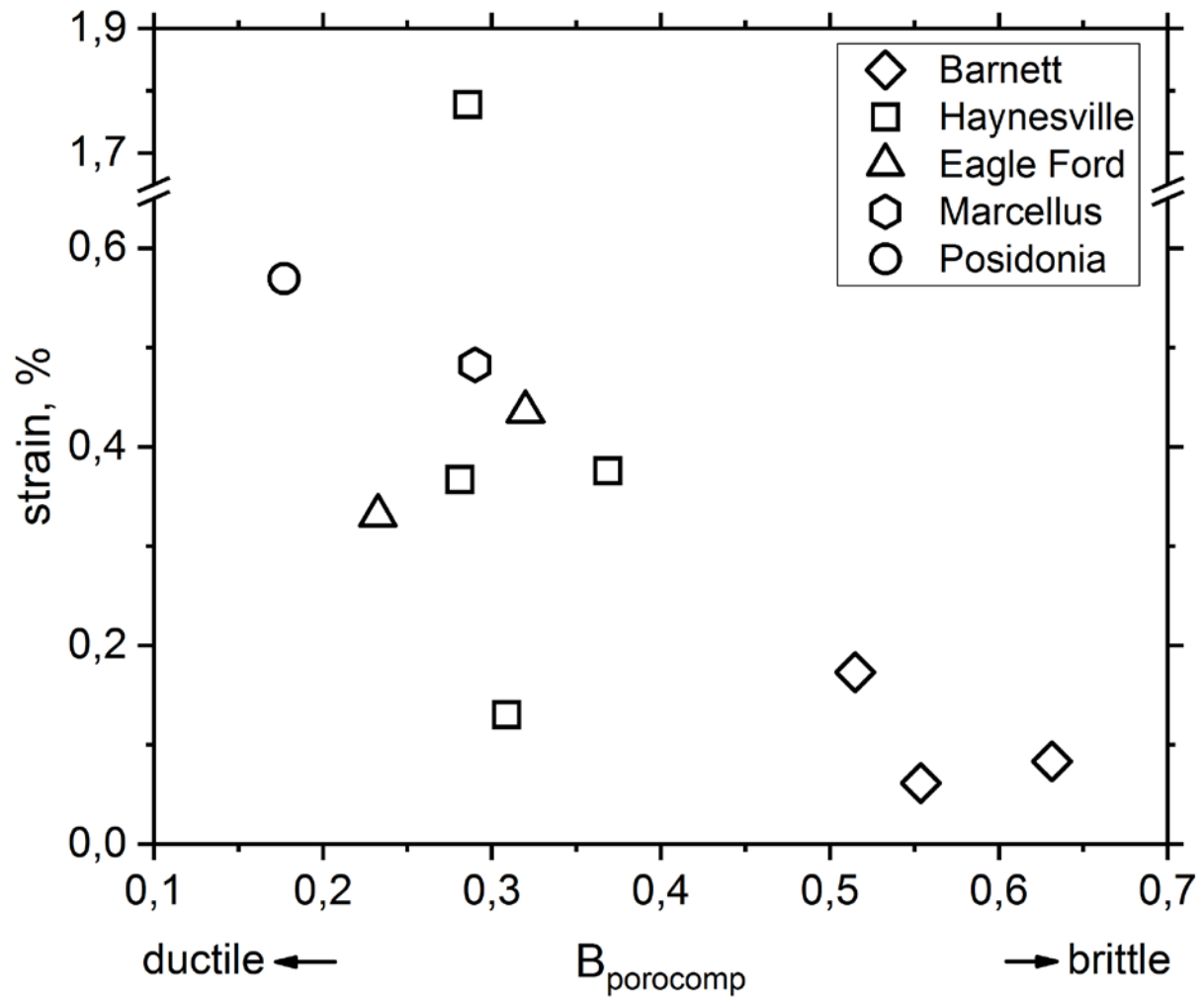


Figure 9: Creep strain (in %) after 3 years deformation at 30 MPa stress and 20°C temperature, 20 MPa pressure versus brittleness ($B_{porocomp}$) determined from composition. Data of American shales are mean values estimated from data published Sone and Zoback (2014), Li and Ghassemi (2012), and Rassouli and Zoback (2015).